Coseismic slickenlines record the emergence of multiple rupture fronts during a surface-breaking earthquake

Clarrie Macklin [a], Yoshihiro Kaneko [a,c,*], Jesse Kearse [a,b]

[a] *GNS Science, 1 Fairway Drive, Lower Hutt, New Zealand*
[b] *Victoria University of Wellington, Kelburn Parade, Wellington, New Zealand*
[c] *Graduate School of Science, Kyoto University, Kyoto, Japan*

A B S T R A C T

Coseismic changes in slip direction recorded by curved slickenlines on fault surfaces are commonly observed following surface-breaking earthquakes. Such observations represent a dynamic record of seismic slip and may provide a new set of constraints on the evolution of propagating rupture and hence earthquake dynamics. We test this hypothesis by conducting dynamic rupture simulations of the 2011 M_w 6.6 Fukushima-Hamadori Earthquake (Japan). These simulations aim to reproduce the well-documented field observations of curved slickenlines that formed during coseismic fault displacement at the ground surface. We consider relatively simple dynamic rupture models with a dipping fault embedded into a homogeneous or layered elastic halfspace. Among a wide range of model parameters tested, we find a model with shallow (<1.5 km) low-velocity layers derived from a regional 3D velocity model combined with a depth-dependent prestress result in curved slip trajectories that closely match slickenline observations. This same model also generates a slip distribution and rupture propagation direction consistent with published inversions constrained by seismological and geodetic data. Furthermore, the characteristics of slickenline curvature are consistent with theoretically predicted earthquake rupture direction. Unlike previous theoretical studies, coseismic changes in rake angle occur due to the emergence of multiple slip fronts within the shallow low-velocity medium. Our results indicate that on-fault geological observations can supplement seismological studies of earthquake rupture evolution beyond traditional datasets.

1. Introduction

Understanding how earthquake rupture propagates over a fault and breaks the Earth's surface is critical for fault displacement and ground-motion hazard assessment. Yet, observations of rupture propagation at shallow depths are elusive, and interactions between earthquake rupture and the free surface are not well constrained. Previous studies argue that details of rupture propagation at shallow depths greatly influence strong ground motion close to the fault trace as well as the resulting fault displacement (e.g., Somerville, 2003; Kaneko et al., 2008; Pitarka et al., 2009). While geodetic data, such as InSAR and optical image correlation, can be used to measure total fault offset at shallow depths (within the top 2–3 km) with high spatial resolution (e.g., Fialko et al., 2001; Dominguez et al., 2003), they are unable to capture the temporal evolution of fault slip during an earthquake. Likewise, strong-motion seismometers and high-rate GNSS receivers, while providing the temporal resolution necessary to constrain the dynamics of coseismic

fault displacement at shallow depths, are usually situated too far from the fault (Fukuyama and Suzuki, 2016; Kaneko et al., 2017) to satisfactorily resolve temporal slip behaviour (at least several hundred meters away). Such records are instead dominated by seismic energy radiation from seismogenic depths. Alternative approaches to study shallow fault rupture processes include the use of dynamic rupture simulations to theoretically examine the consequences of free-surface-induced rupture phenomena (e.g., Aagaard et al., 2001; Kaneko et al., 2008; Kaneko and Lapusta, 2010; Hu et al., 2019). However, simulated rupture scenarios are strongly dependent on model assumptions (e.g., Aagaard et al., 2001; Kaneko et al., 2008; Kaneko and Lapusta, 2010; Hu et al., 2019), and it is unclear which conditions are more physical than others. Therefore, resolving both the kinematics and dynamics of rupture propagation within the shallow portion of a fault remains a major challenge in seismology.

Changes in coseismic slip direction captured as striations on fault surfaces, referred to as slickenlines, are commonly documented after

---

surface-breaking earthquakes (e.g., Otsuki et al., 1997; Otsubo et al., 2013; Kearse et al., 2018, 2019) and may provide direct constraints on time-dependent fault movement at shallow depths. However, interpreting observed slickenlines is not straightforward because many slickenlines created by large earthquakes are either curved, mismatched to the overall slip, or overlap each other (Kearse et al., 2019; Kearse and Kaneko, 2020). As a result, interpretations of curved slickenlines have often relied on complex and earthquake-specific mechanisms, such as slip aligning with the regional stress direction calculated from stress tensor inversion of events following a mainshock (Otsubo et al., 2013), cumulative slip of two discrete rupture episodes with different slip directions (Avagyan et al., 2003), and complex stress interactions near the

junctions of intersecting faults (Xu et al., 2013).

Alternatively, Spudich et al. (1998) and Guatteri and Spudich (1998) proposed that temporal changes in rake angle may be driven by dynamic stresses on the sliding fault surfaces. In particular, such transient stress changes occur within the fault's process zone (i.e., the area of the fault surface undergoing a transition from static to dynamic friction) that contribute to rake rotation during slip (Mizoguchi et al., 2012; Otsubo et al., 2013; Kearse et al., 2019; Guatteri and Spudich, 1998). Dynamic fault rupture models demonstrate that transient stresses at the crack tip can cause initial slip directions misaligned with initial prestress (to which the slip direction eventually tends to) (Andrews, 1994; Guatteri and Spudich, 1998; Bizzarri and Cocco, 2005). Kearse et al. (2019)
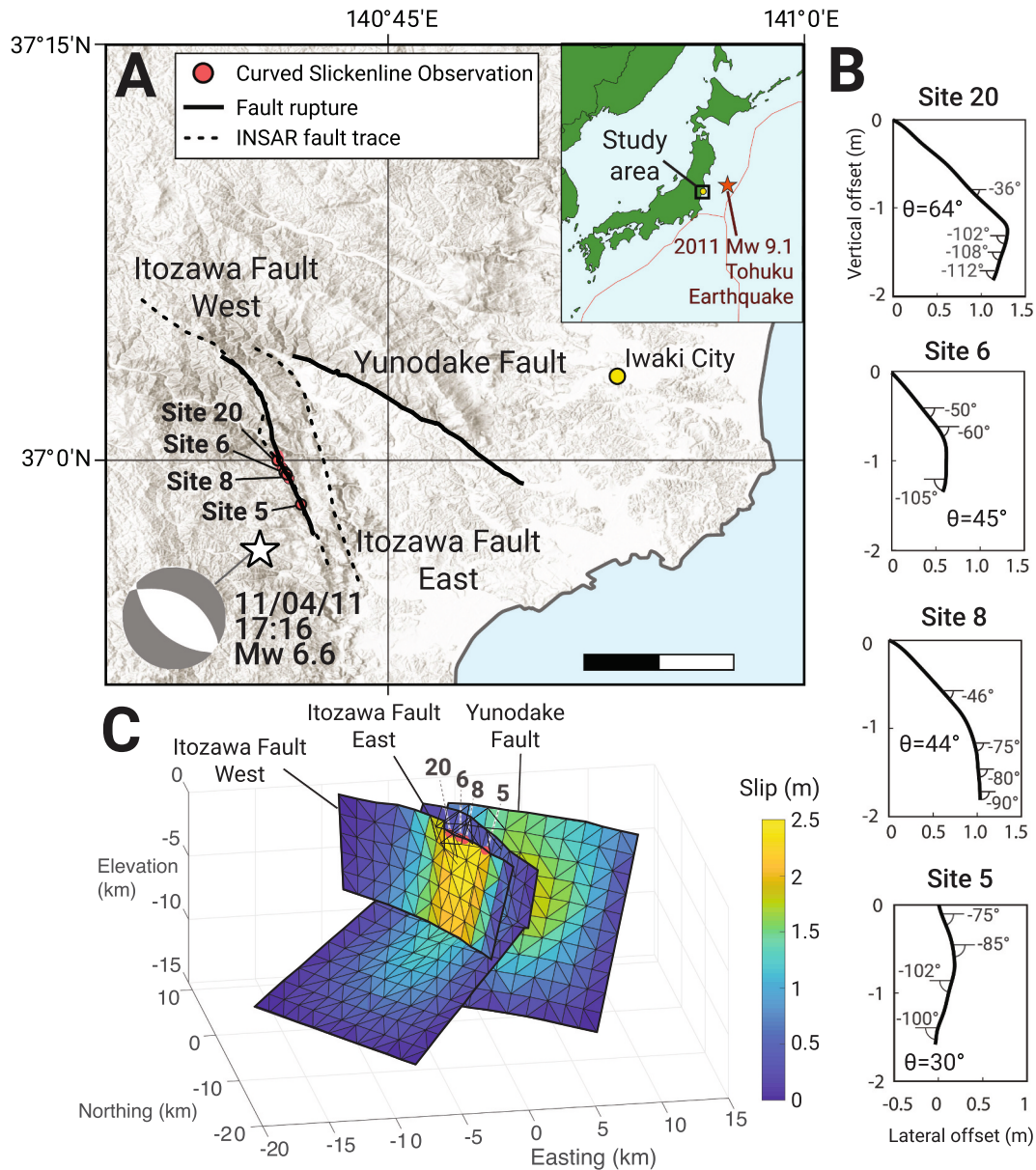
Fig. 1. (A) A map of the study area with an inset showing the proximity to the $M_w = 9.0$ Tohoku mainshock. The focal mechanism for this event implies normal faulting with a small component of left-lateral displacement. Rupture originated near the southern end of the Itozawa fault (the epicentre is shown by the white star). Solid black lines delineate documented fault rupture from Mizoguchi et al. (2012). These align with discontinuities observed in interferograms (marked by dashed lines) which Fukushima et al. (2013) use to define the upper surface (i.e., $z = 0$ m) of fault geometries shown in C. Curved slickenlines recorded by Mizoguchi et al. (2012) along the Itozawa West fault are marked by red circles. (B) Four slickenline reconstructions are presented by Otsubo et al. (2013). Rake angles use the convention of 0° pointing along-strike to the southeast and negative values are down-dip (corresponding to normal slip). The total change in rake angle θ is displayed in each plot. The position of maximum curvature in the slip path occurs later and net rake angle change increase with distance down-fault from the hypocentre. (C) The inversion for slip magnitude and fault geometry produced by Fukushima et al. (2013) shows that slip mainly occurred on the Itozawa West Fault. (For interpretation of the references to colour in this figure legend, the reader is referred to the web version of this article.)

demonstrated that slickenline curvature observed along the Kekerengu Fault following the 2016 M_w 7.8 Kaikoura Earthquake (New Zealand) is consistent with this mechanism and further hypothesised that slickenline curvature could preserve the rupture propagation direction of past earthquakes. Kearse and Kaneko (2020) analysed historical earthquakes that produced curved slickenline and in each case, slickenline curvature is consistent with an idealised dynamic rupture model that uses the event's rupture direction and kinematics. However, their models have only been applied to recreate the sense of convexity of slickenline observations (e.g., convex up or convex down) (Kearse et al., 2019; Kearse and Kaneko, 2020); no attempt has been made to reproduce other available constraints, such as the detail of the slickenline path, measured slip across the fault, and geophysical observations such as the distribution of slip and moment magnitude. Modelling these additional slickenline features and geophysical constraints would help evaluate the physical robustness of the numerical modelling framework proposed by Kearse and Kaneko (2020).

This study aims to establish a more comprehensive link between slickenline curvature and fault rupture processes (including rupture direction), and thereby maximise the potential for extracting information on earthquake rupture evolution from geological observations. In Section 2, we describe a rich and well-documented catalogue of curved slickenlines generated during the 2011 M_w 6.6 Fukushima-Hamadori Earthquake. Also, we compile geophysical observations that constrain the earthquake parameters. In Section 3, we describe the dynamic rupture model setup and assumptions. Section 4 compares model outputs to slickenline observations and a geodetically-derived slip distribution at the surface and at depth. In addition, we explore the sensitivity of the rupture process and resulting slickenlines to the choice of model parameters. In Section 5, we discuss the implications of our results for interpreting coseismic slickenline observations and their potential for constraining rupture evolution at shallow depths.

2. Earthquake setting

The April 11 M_w 6.6 Fukushima-Hamadori Earthquake produced fault scarps from which detailed curved slickenline observations are obtained (Fig. 1; Mizoguchi et al., 2012; Otsubo et al., 2013). The M_w 6.6 event is the largest in a series of normal faulting aftershocks in the Fukushima and Hamadori precincts triggered by the 11 March M_w 9.0 Tohoku-Oki Earthquake (Imanishi et al., 2012; Fukushima et al., 2013). Before the Tohoku-Oki earthquake, shallow (<15 km) seismicity in the Fukushima-Hamadori region was low-magnitude and relatively quiescent compared to surrounding districts in Eastern Honshu (Imanishi et al., 2012). The Tohoku-Oki mainshock is thought to have enhanced extensional stresses in the region and primed existing normal faults for failure (Toda et al., 2011; Okada et al., 2011; Kato et al., 2011; Yoshida et al., 2015; Otsubo et al., 2018). The Fukushima-Hamadori Earthquake involved multiple faults including the Itozawa fault and Yunodake fault (Fig. 1; Mizoguchi et al., 2012). The Itozawa Fault broke into eastern and western strands. The majority of observed vertical offsets are documented from on the Itozawa West fault, with maximum displacements of ~2 m. The nearby Yunodake fault produced a maximum vertical offset of 0.9 m (Mizoguchi et al., 2012).

Fault geometry and coseismic slip distribution on faults activated during the Fukushima-Hamadori Earthquake are constrained by InSAR and geological field observations (Fukushima et al., 2013; Mizoguchi et al., 2012). The resulting slip distribution shows that most of the slip is shallow (<5 km depth) and is concentrated on the Itozawa West fault, where peak slip is 2.7 m (Fig. 3C). Other slip distributions from InSAR observations and waveform modelling also suggest that slip is concentrated in the upper 5 km of the crust (Kobayashi et al., 2012; Hikima, 2012).

The rupture process during the Fukushima-Hamadori Earthquake is complex: the event involved coseismic rupture transfer across two sub-parallel faults unconnected at the surface (Toda and Tsutsumi, 2013;

Fukushima et al., 2013). Kinematic waveform models suggest the two faults broke in succession (Hikima, 2012; Kobayashi et al., 2012; Tanaka et al., 2014). Rupture initiated in the southeast corner of the Itozawa West Fault, propagated to the northwest, and triggered a southeast-directed rupture on the Yunodake fault. According to Tanaka et al. (2014), for a short time (7 s) before rupture on the Itozawa West had terminated, both faults were slipping simultaneously. Tanaka et al. (2014) argue that rupture along the Itozawa fault induced crustal stress changes sufficient to nucleate secondary rupture on the Yunodake fault. While kinematic models help provide a well-defined rupture direction for the event, no dynamic model has been created for the Fukushima-Hamadori Earthquake.

Curved slickenlines were observed along a ~4 km extent of the Itozawa West Fault (Fig. 1; Mizoguchi et al., 2012; Otsubo et al., 2013). Where slickenline curvature is observed, slip paths show a single bend (change in slip rake angle) which, in some cases, results in overlapping slickenline tracks (Fig. 1B). Slip paths can generally be divided into upper (i.e., earlier) and lower (i.e., later) segments which represent initial and final slip directions (Otsubo et al., 2013). As a broad trend, both the magnitude of rake angle change (measured in degrees) and the length of the upper segment with respect to the total slip length tend to increase with distance northwest along strike from the hypocentre (Fig. 1B).

3. Methods and model setup

We use dynamic fault rupture simulations to replicate features of Itozawa West Fault slickenlines using a combination of geological, geodetic, and seismological constraints. Our model considers the propagation of spontaneous rupture on an 18-km by 7-km fault plane embedded within a three-dimensional elastic medium (Fig. 2A). The modelled fault plane dips at 75° to match the nominal fault dip suggested by the fault geometry derived from an inversion of coseismic interferogram (Fig. 1C; Fukushima et al., 2013).

Elastodynamic behaviour along the fault surface is modelled by defining a split-node boundary where traction is continuous, but slip is permitted (Kaneko et al., 2008). The relationship between traction and slip is governed by a linear slip-weakening friction law: once the fault fails, shear stress decreases from its static value τ_S to its dynamic value τ_D over some characteristic slip distance D_C (Ida, 1972; Palmer and Robert Rice, 1973). The fault's static strength is governed by failure criteria $\tau_S = \mu_S \sigma_N + C$ where σ_N is effective stress, μ_S is the static friction coefficient, and C is the frictional cohesion. The dynamic shear stress is given by $\tau_D = \mu_D \sigma_N$ where μ_D is the coefficient of dynamic friction. We assume that slip velocity is parallel to shear traction at each instant at all fault nodes (e.g., Bizzarri and Cocco, 2003). Following this assumption, we calculate slip rake angle based on the ratio of velocity components $\theta = tan^{-1}\left(\frac{V_z}{V_x}\right)$ (Andrews, 1994). The fault is initially at rest, and dynamic rupture is initiated by imposing a smooth, time-dependent rupture within a 3-km nucleation patch centred on the hypocentre (white star in Fig. 2A). The details of the nucleation procedure are described in benchmark problem TPV22 (Harris et al., 2018) (http://scecdata.usc.edu/cvws/). Once rupture nucleates, it propagates spontaneously outside the nucleation patch. The elastodynamic behaviour, i.e., the equations governing the fracture and subsequent fault motion, is determined using the spectral element solver (Ampuero, 2002; Kaneko et al., 2008), which has been verified through a series of community benchmark exercises (Harris et al., 2009, 2018).

The sense of modelled surface slip is affected by fault geometry and initial stress direction. Following Kearse et al. (2019), initial normal and shear stresses are uniform along strike but increase linearly with depth to account for diminishing confining stresses towards the surface (Fig. 2B). Furthermore, to reproduce the sense of curvature in observed surface slip, we approximate fault prestress using the focal mechanism of Fukushima-Hamadori event as a broad approximation to the
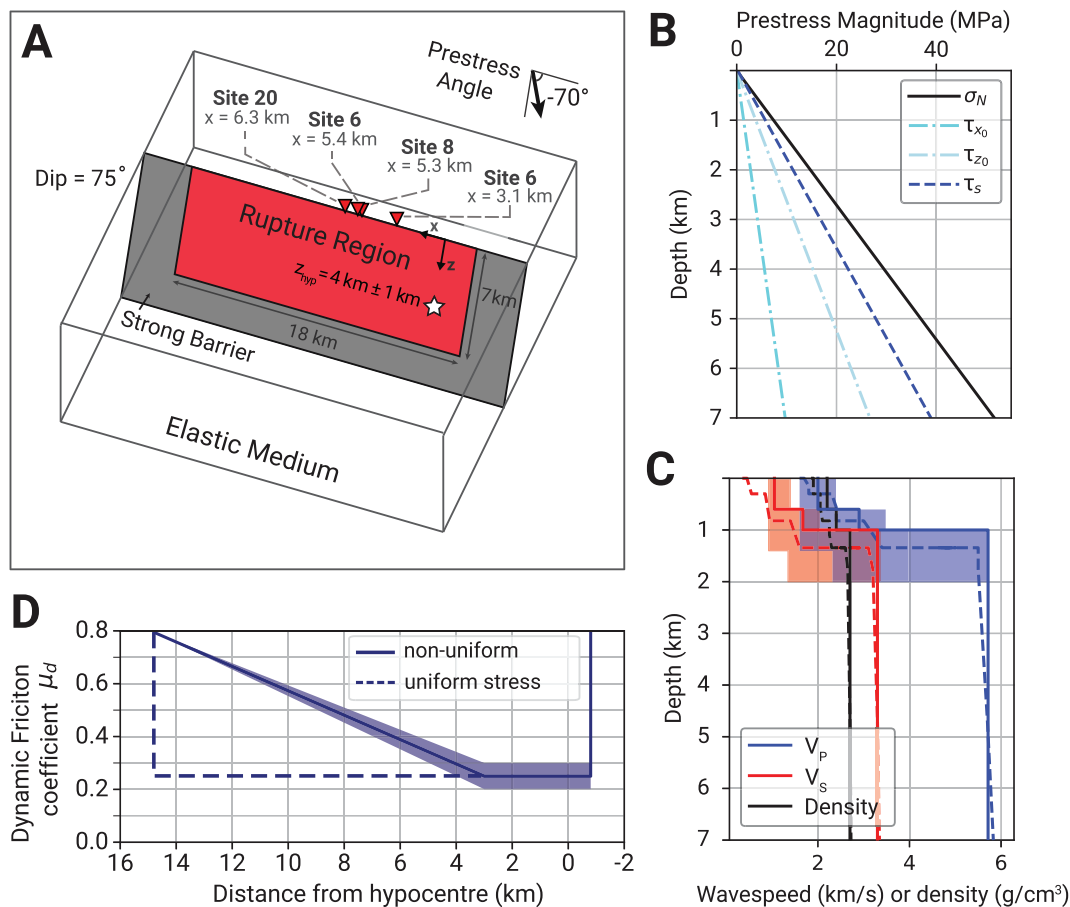
Fig. 2. A summary of the dynamic rupture model setup. (A) A fault surface is embedded within an elastic half-space to represent the Itozawa West Fault. Rupture is initiated by a nucleation path (shown by the white star). To confine rupture propagation within the rupture region, a strong barrier with an arbitrarily high static friction coefficient surrounds the rupture zone. (B) The initial stress state along the fault surface is governed by linearly-increasing effective stress σ_N which implies the stress required to break the fault τ_S tends to zero at $z = 0$ m. The prestress angle influences the initial shear traction components in the plane of the fault (τ_{x0} and τ_{z0}). (C) To model the effect of local velocity structure on earthquake rupture we use a three-layered velocity model with two shallow layers overlying a half-space. The dashed line shows the values interpolated from a regional 3-D velocity model (Fujiwara et al., 2012). Solid lines show the favoured 1-D velocity structure used for the preferred model in Figs. 3B, 5, and 6. The solid shading surrounding the P- and S-wave speeds represent the range of velocities and layer thicknesses explored in this study. (D) Dynamic friction increases linearly across the fault such that rupture arrest towards the opposite end of the fault. Although dynamic friction increases linearly along strike such that rupture arrest towards the opposite end of the fault, a case with uniform dynamic friction does not significantly affect the slickenlines' net rotation).

background stress field (Fig. 1A). The focal mechanism implies a normal faulting event with a small component of strike-slip from which we set an initial stress direction with a rake of $-70°$ in the fault plane (Figs. 1, 2A). Rake in this study is negative down-dip and 0° points horizontally southeast along the Itozawa fault (Fig. 1).

The slip distribution provided by Fukushima et al. (2013) constrains the spatial extent of modelled rupture and the resulting moment magnitude (Fig. 1C). We focus on the Itozawa West Fault only, and the corresponding moment magnitude of this fault segment from the InSAR-derived model is $M_w = 6.38$ (Fukushima et al., 2013). This slip distribution was derived using a fixed rake angle meaning that lateral slip is not considered. Nevertheless, the Fukushima et al. (2013) model provides a representation of the magnitude and distribution of slip and one which we aim to reproduce.

As well as matching a slip distribution, we constrain modelled surface slip using slickenline reconstructions displayed in Fig. 1B (Otsubo et al., 2013). While other slickenline curvature observations were made on the Itozawa West Fault, these four sites are the only outcrops where striations of sufficient length are available to project a slip trajectory between the up-thrown and down-thrown blocks (Otsubo et al., 2013). The main modelling objective is to replicate the overall characteristics of slickenlines. Firstly, the modelled surface slip should resemble the shape

of recorded slickenlines – i.e., modelled slip should include a sharp change in slip direction within the latter half of the slip path. Secondly, we aim to reproduce the magnitude of net rake rotation at each site and hence the spatial variation in rake rotation with distance along-strike. These two criteria are emphasised because changes in total offset over short distances are unlikely to occur in our relatively simple model (e.g., Sites 6 and 8 are a few hundred metres apart but have significantly different offsets). We focus instead on the slip rake angle changes and their position in the slip path as the most robust measurements for qualitatively assessing our model's fit to observations.

Model parameters μ_D, μ_S, C, and D_C are tuned to control the size and duration of dynamic stress drop across the fault and, in turn, influence the speed and strength of rupture (Table S1, S2). For simplicity, we assume that static friction, characteristic slip length, frictional cohesion, and prestress are uniform along strike. Modelled slip paths are compared to slickenlines at four sites along the fault surface which have similar along-strike distances from the hypocentre (see Fig. 1B). To account for a ~1 km uncertainty in hypocentre depth in the JMA hypocentre location, we vary the depth where rupture originates z_{hyp} between 3 km to 5 km.

Depth-dependent seismic wavespeed in the vicinity of the Itozawa fault, evident in a 3-D regional velocity model of Japan (Koketsu et al.,

2012), could influence modelled rupture dynamics and slickenline shape. To test the effect of non-uniform seismic wavespeed on rupture dynamics and its influence on surface slip, we consider cases for elastic mediums with homogeneous seismic wavespeed and a three-layered velocity model comprised of two shallow low-velocity layers overlying a half-space (henceforth referred to as "homogeneous" and "layered" models in this study). The seismic wavespeed for each layer is set to best match a 1-D structure for compressional and shear wave speeds (V_P, V_S), and density ρ interpolated from the 3-D regional velocity (see dashed lines in Fig. 2). We vary V_P and thickness d of the upper two layers to test the effect on coseismic rake angle changes at the surface. The filled area of Fig. 2C shows the parameter space of seismic wavespeed and layer thickness explored in this study. The seismic wavespeed for the homogeneous model is set using V_P, V_S, and ρ from the half-space layer.

4. Results

4.1. Homogeneous velocity case

Models that assume depth-dependent prestress and homogeneous velocity structure reproduce net rake angle change at all sites while attaining a comparable slip distribution to the InSAR-derived solution (Fig. 3A, C); however, homogeneous models are unable to replicate the detailed shape of slickenline observations. Fig. 3A shows surface slip from our preferred homogeneous model which best reproduces the increase in curvature with distance from the hypocentre: net rake rotation grows from $\theta = 34° \pm 5°$ at Site 5 ($x = 3.1$ km) to $\theta = 53° \pm 5°$ at Site 20 ($x = 6.3$ km) (see supplementary material for explanation of net rake change calculation). The initial and final slip directions are well modelled for Site 8, while the final slip direction for Sites 5 and 20 are underestimated by 27° and 15° respectively (Fig. 3A). Apart from Site 20, observed rake rotation (black curves in Fig. 3) fits within the range of modelled net rake angle change. Additionally, the sense of curvature is insensitive to the choice of friction parameters in the range explored (Table S1).

For the range of parameters tested, the majority of rake angle change consistently occurs near the slip path's origin and varies smoothly. No choice of parameters resulted in rake angle changes occurring in the latter half of the slip path (Fig. 3A). Consequently, for Sites 8 and 20, the model does not accrue enough horizontal slip to match the observed component of strike-slip offset. The initial modelled displacement at all sites is mostly strike-slip: plots of rake angle versus time (Fig. 4B) show an area of weak slip leading the main rupture front characterised by an enhanced horizontal displacement component (red colours in Fig. 4A). However, the displacement from this early slip episode accounts for only a small fraction of the total slip path (Fig. 4). As the main front arrives, horizontal stresses peak and decrease to zero, slip rate accelerates, and rake angle rotates clockwise by ~50° (Fig. 4C). Once the main front has passed, an area of near-vertical rake covers the upper 1 km of the model (blue colours in Fig. 4B). Rake angle change primarily occurs within the process zone (marked by the vertical black line in Fig. 4A), which is consistent with the model prediction of Spudich et al. (1998), Kearse et al. (2019), and Kearse and Kaneko (2020).

4.2. Layered velocity case

To better explain features of curved slickenline observations, we consider dynamic rupture simulations within a layered velocity medium with depth-dependent prestress. A model with two low-velocity layers that overly a half-space provides surface slip that more closely resembles the broad characteristics of slickenline observations from the Fukushima-Hamadori Earthquake (Fig. 2C, 3B). As in the homogeneous model, our preferred layered velocity model broadly captures an along-strike increase in net rake angle change with distance from the hypocentre: net rake rotation increases from $\theta = 26° \pm 4°$ at Site 5 ($x = 3.1$ km) to $\theta = 48° \pm 3°$ at Site 20 ($x = 6.3$ km). Remarkably, the

layered model produces a rapid change in curvature within the latter half of the slip path, resulting in a dogleg shape for Sites 6, 8, and 20 (Fig. 3B).

The initial slip direction is better reproduced than the final slip direction. The slip rake angle for Sites 6, 8, and 20 is within ~5° during the first ~0.5 m of slip (Fig. 3B). At Site 20, the final slip direction is underestimated by 21° (Fig. 3B). This deficit in rake rotation is consistent across all layered models tested: for no choice of parameters could right-lateral slip observed at Sites 5 and 20 be reproduced assuming a prestress angle of $\theta_0 = -70°$. While modelled slip at Site 6 reproduces the initial and final slip directions, the length of the upper and lower slip path segments is longer than observations suggest (Fig. 3B). Like the preferred homogeneous model, net rake angle change at Site 5 is reproduced, but neither the position of rake angle change nor the initial slip direction at this site can be recreated for any parameter choice (Table S2).

The second minor kink near slip termination (blue arrow in Fig. 3B) is influenced by stopping phases arriving from rupture arrest at the fault's edge which carries opposing stresses to the main rupture front (Fig. 3B). This effect is enhanced when shallow velocity layers are introduced (compare Fig. 3A and B).

The preferred layered model's slip distribution better resembles the InSAR-derived slip distribution compared to the homogeneous case (Fig. 3). The area of largest slip magnitude (~2.5 m) is confined to the low-velocity zone (where $z \leq 1$ km), bringing peak slip closer to the surface. Our rupture model produces a moment magnitude $M_w = 6.32$ and a peak slip of $D_{max} = 2.4$ m. This moment magnitude and peak slip are consistent with $M_w = 6.38$ and $D_{max} = 2.7$ m from the InSAR-derived slip model for the Itozawa West fault (Fukushima et al., 2013).

For the layered model, a lengthened upper (i.e., earlier) slip path segment and sharp rake angle change are both facilitated by the arrival of two slip fronts near the surface. The first slip-rate peak arrives as the main rupture reflects off the free surface, constructively interferes with the main rupture front at depth, and enhances slip rate (Fig. 5). As in the homogeneous case, the first slip episode carries enhanced horizontal stresses in the upper 2 km causing displacement oblique to the prestress direction (Fig. 4). Following the first slip rate peak, a short (0.25 s) decrease in slip rate occurs before a second peak arrives. This second peak is accompanied by a deviation in traction components: vertical stresses increase, and horizontal stresses tend towards zero (Fig. 6). A sharp kink in the slickenline forms during the transition between the two slip rate peaks where rake angle rotates 45°. After the rupture front passes, rake angles along the free surface range from −80° to −120°.

The broad characteristics of the observed slickenline curvature, i.e., the majority of slip direction change occurring late in the slip path resulting in a dogleg shape, are mainly confined to the upper few hundred meters. Fig. 6B shows modelled slip at depths of 0 m, 100 m, 200 m, 500 m, 700 m and 1 km at $x = 6.3$ km (Site 20). By $z = 500$ m the intensity of slip path curvature has diminished significantly, and most of the slip direction changes occur early in the path. Even at $z = 200$ m, the kink is broader and smoother. Slip at $z = 100$ m, however, contains largely the same features as slip at the free surface. Hence, it gives a close representation of surface fault motion observed (Fig. 6). At depths below 2 km, slip directions remain close to the prestress angle $\theta_0 = -70°$ throughout the rupture process.

4.3. Parameter sensitivity

To explore the sensitivity of surface slip to model parameters that are not well constrained from geophysical observations, we vary seismic wavespeeds in the low-velocity medium, low-velocity-layer thickness, dynamic friction coefficient μ_D, characteristic slip length D_C, and hypocentre depth z_{hyp} using the preferred layered case as a reference (Fig. 3B, 5, and 6).

Varying the model's velocity structure changes the magnitude and position of slip path curvature. A decrease in shallow layer seismic
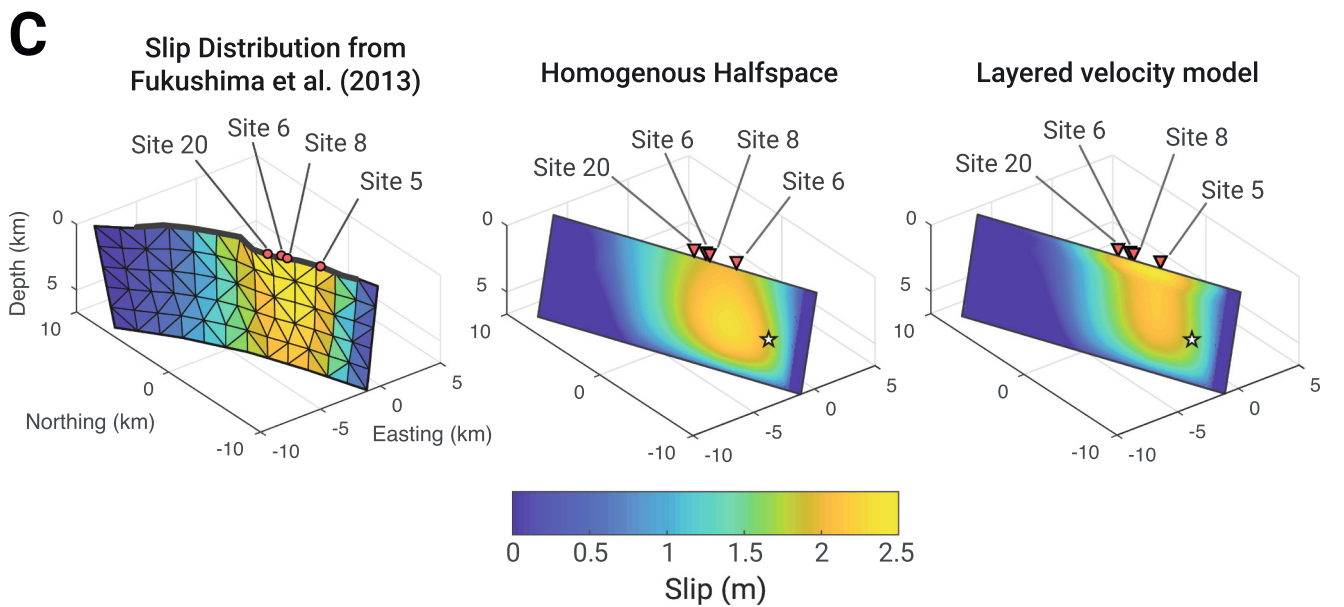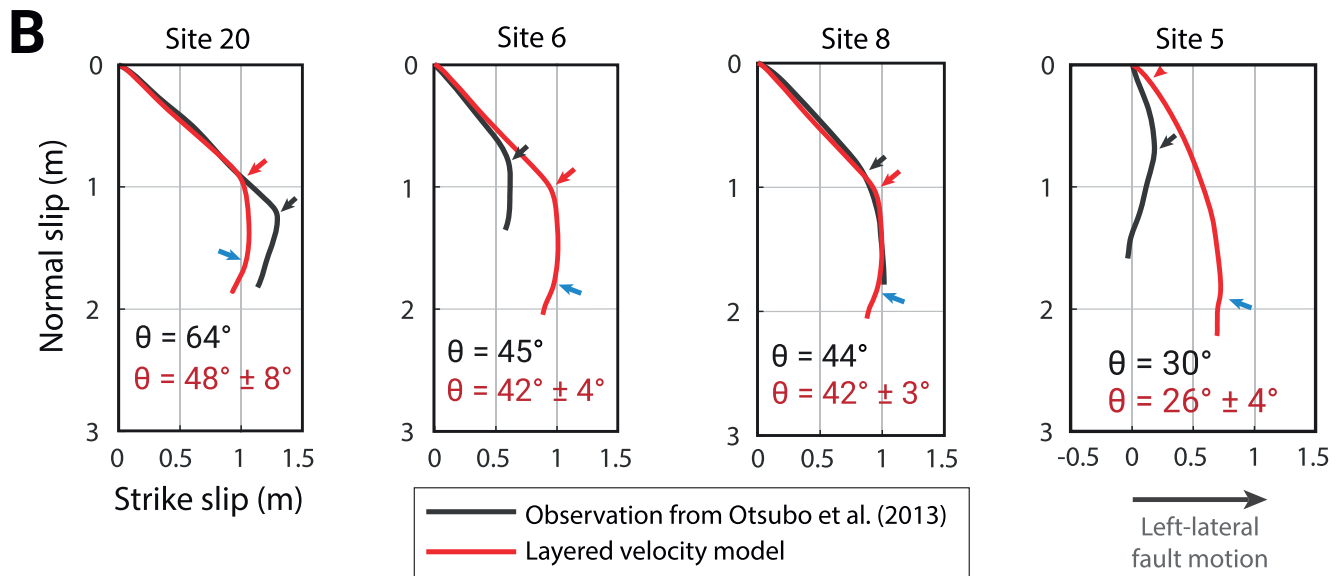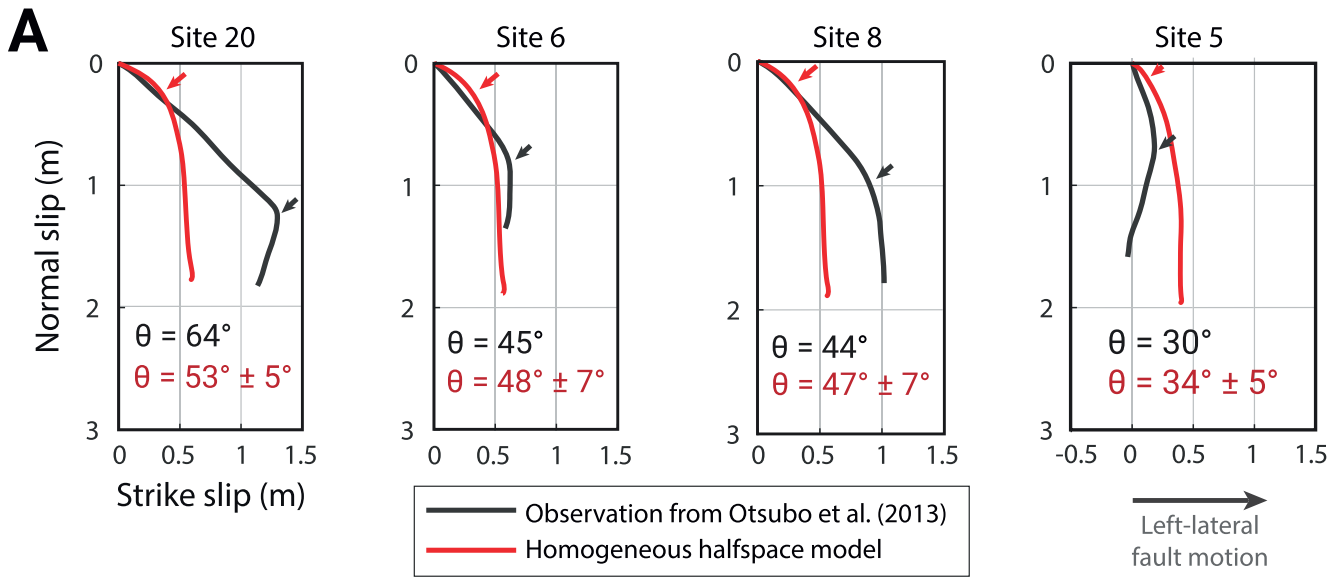
(caption on next page)

Fig. 3. (A) A plot of surface slip from the preferred model with homogeneous velocity structure (red line) versus the slickenline reconstructions from Fig. 1B (black line). Net rake rotation for the observed slickenline and the modelled solution at each site is displayed below each slip path. Red and grey arrows mark the position of maximum slip direction change for the model and observations, respectively. (B) The same comparison in A is repeated for the preferred layered velocity model solution. The maximum change in rake angle change is sharper and located closer to observations. The second kink in the slip path (shown by the blue arrow) is influenced by the model's stopping phase and rupture front reflections. (C) Total slip from homogeneous and layered velocity cases are compared to the Fukushima et al. (2013) slip distribution. Overall, the model with a layered velocity structure provides a better fit to slickenline and slip distribution constraints. (For interpretation of the references to colour in this figure legend, the reader is referred to the web version of this article.)
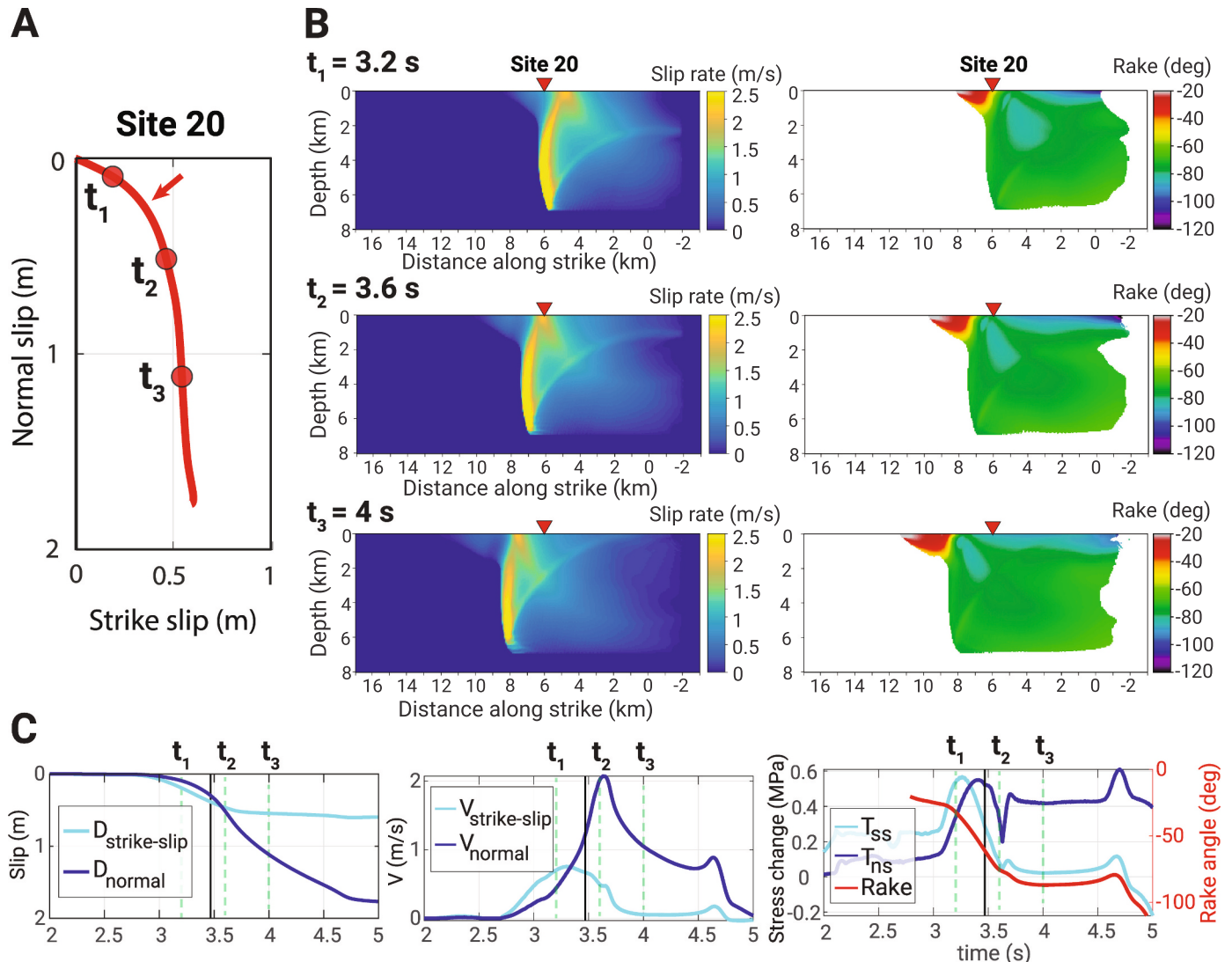
Fig. 4. Fault variables plotted for the homogeneous seismic wavespeed model. This model uses $\mu_S = 0.75$, $\mu_D = 0.2$, $D_C = 50$ cm, $C = 0.2$ MPa, and $z_{hyp} = 4$ km. (A) A plot of slip history at Site 20 with three time markers show that the majority of rake angle change occurs between t_1 and t_2 early in the slip path. (B) Three snapshots are plotted for slip rate (m/s) and rake angle (deg) which show a weak episode of slip ahead of the main front (t_1), during peak slip (t_2), and following peak slip (t_3). The red triangle marks the position of Site 20 where plots in C are made. After the main front passes, rake becomes near vertical in the upper 1 km of the model. (C) Plots of slip (m), slip rate (m/s), and shear traction change $\Delta\tau$ (MPa) from 100 m below Site 20 show that slip direction change occurs early in the slip path between (t_1) and (t_2). Note that on-fault quantities at surface sites and sites 100 m below are very similar (Fig. 6B). To avoid plotting numerical oscillations, the rake is smoothed using a running mean with a window size of 0.2 s. (For interpretation of the references to colour in this figure legend, the reader is referred to the web version of this article.)

wavespeed lessens net rake angle change. When V_P is decreased by 20% in the upper two layers, slip at Site 20 undergoes $35°\ \pm 6°$ of rake rotation compared to $51°\ \pm 3°$ for the higher velocity case (Fig. 7). The difference in net rake rotation is associated with a change in rupture front shape and speed near the surface. Rupture speed decreases in slower layers which causes a bend in the slip front at the boundary between the low-velocity layers and the underlying halfspace. Bending of the rupture front causes a reduction in strike-slip-oriented dynamic stresses, resulting in an initially steeper rake angle. Additionally, a reduced wave speed within the low-velocity layers results in an increased separation between the two rupture fronts, which in turn lengthens the upper segment of the slip path (Fig. 7A).

Modelled slip path curvature is most sensitive to the uppermost layer's seismic velocity. Changing seismic wavespeed in the middle layer causes only minor changes to total surface slip and rupture front shape (Fig. 7A). Overall, there is a trade-off between increasing coseismic rake angle rotation (by increasing shallow layer seismic wavespeed) and causing the "kink" to occur closer to the slip path's origin.
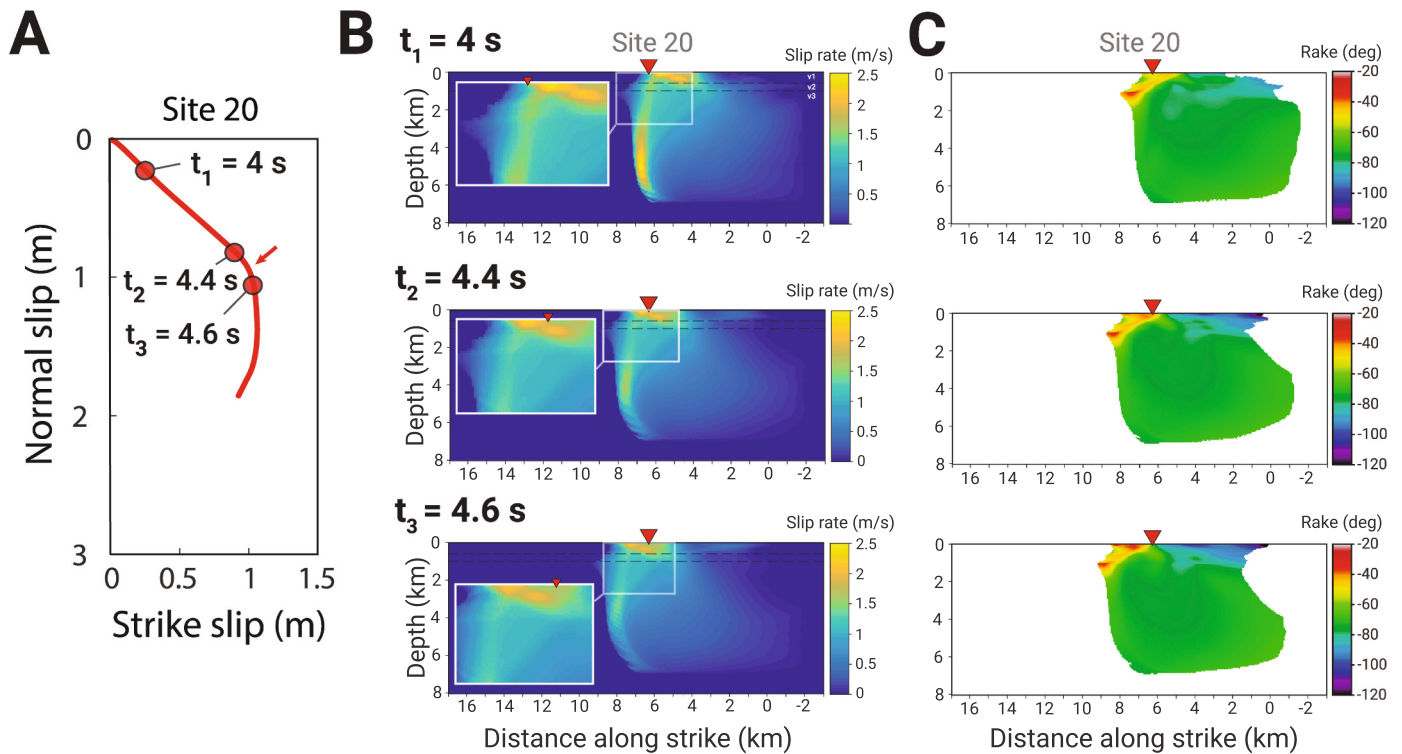
Fig. 5. Plot of slip history, slip rate, and rake angle for the preferred layered case. The same friction law parameters and hypocentre depth is used as the homogenous case in Fig. 4, except $\mu_D = 0.25$. (A) A plot of slip history at Site 20 with three time markers show that the majority of rake angle change occurs between $t_2 = 4.4$ s and $t_3 = 4.6$ s. (B) Snapshots of slip rate show a concentration of slip rate near the free surface: a bright slip front following the first peak is reflected rupture. Insets show a second, more diffuse slip front follows the reflected slip front near the surface. (C) Plots of rake angle show that stresses have significant horizontal components near the crack tip. Following the main rupture front, the stress field orientates to near-vertical (light blue colours). Large changes in slip direction are confined to the shallow velocity layers. Here, we plot rake using the velocity components to capture slip direction changes. To only show the moving portion of the fault, we mask rake angle where $|V| < 0.1$ ms^{-1}. (For interpretation of the references to colour in this figure legend, the reader is referred to the web version of this article.)
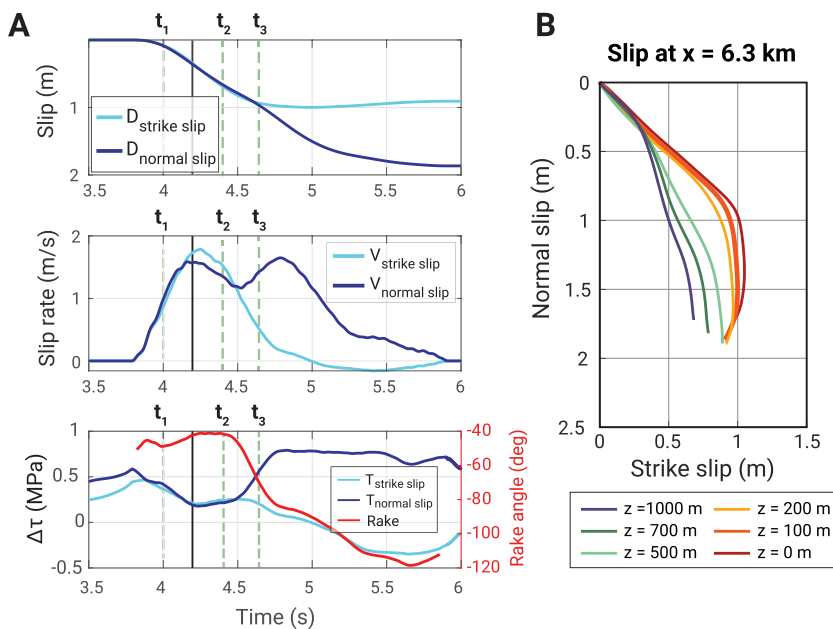
Fig. 6. Plots of fault variables for the preferred layered velocity model shown in Fig. 5. (A) Slip (m), slip rate (m/s), shear traction change $\Delta\tau$ (MPa), and rake (deg) is plotted 100 m below Site 20. The plot of slip rate (middle) shows two slip fronts of similar magnitude arrive at t_1 and t_3. The first peak carries stresses that are roughly equal in their horizontal and vertical components. Between t_2 and t_3, the second slip front arrives, bringing mostly vertical stresses. The sharp change in slip direction occurs during the transition between the two slip rate peaks. (B) Slip paths in the upper 1 km of the model show that a sharp kink in the latter half of the slip path is only produced in the upper 200 m. Note that the curvature at 100 m is roughly the same as the surface which justifies plotting stresses at this depth to avoid numerical complexities.

Changing low-velocity layer thickness has a similar effect to changing seismic wavespeed but introduces additional complexity into modelled slip paths (Fig. 7D). A thicker shallow low-velocity zone creates longer surface slip paths because of the dynamic amplification of slip and slip rates within the low-velocity layers (e.g., Kaneko et al., 2011). Also, the separation of rupture fronts becomes more pronounced such that, for the thickest low-velocity zone model (Fig. 7F), the near-surface comes to a halt between the first and second slip fronts. The arrival of the second slip front causes a rapid rake angle change. Though, this second front decreases the magnitude of net rake angle change
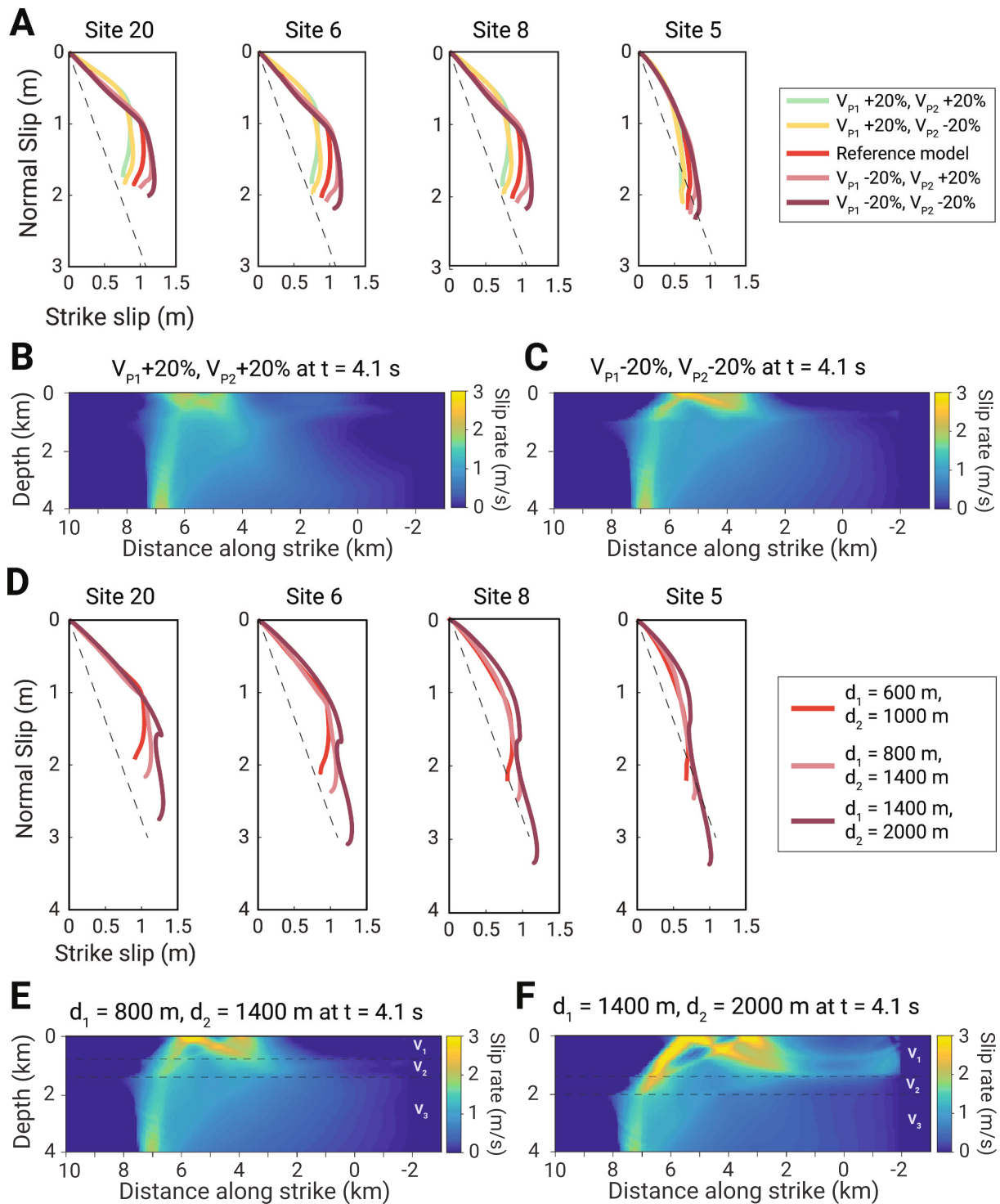
Fig. 7. The effect of changing seismic wavespeed (V_P and V_S) and layer thickness of the low-velocity zone on modelled surface slip. In plots (A) and (D), the red line shows the preferred layered model solution from 3B and the grey dashed lines show in-plane prestress angle ($\theta_0 = -70°$). (A) Plots of surface slip when the thickness of shallow velocity layers is kept constant and the P-wave velocity of each layer is perturbed by $\pm 20\%$. The S-wave velocity is given assuming a Poisson solid such that $V_P = \sqrt{3}V_S$. B and C plot slip rate in the upper 4 km at $t = 4.1$ s. The incidence angle of the slip front changes depending on the velocity contrast between the half-space and the low-velocity layers. (D) Surface slip becomes larger and more complex when layer thickness in increased. E and F plot slip rate in the upper 4 km at $t = 4.1$ s for models with different layer thicknesses. Rupture front bifurcation is intensified and slip rate increases near the surface when layer thickness is increases. (For interpretation of the references to colour in this figure legend, the reader is referred to the web version of this article.)

compared to the preferred layered velocity model; the subsequent stress field contains a significant horizontal component, which drives further strike-slip and leads to a lower net rake angle change between the initial and final slip directions (e.g., Site 20 in Fig. 7D). Overall, the change in

thickness has a limited effect on the position of the slip path kink. Conversely, it has a significant effect on surface slip magnitude, the magnitude of rake angle change, and the strength of shallow rupture fronts (both primary and reflected) that contribute to slip path

complexity.

Decreasing dynamic friction coefficient μ_D or characteristic slip length D_C increases the sharpness of rake angle changes; although, the values tested in this study are unable to induce net rake angle change observed at Sites 5 and 20 (Fig. 8A,1B, 3B). When μ_D is lowered below the preferred layered case values ($\mu_D = 0.25$, $D_C = 50$ cm), the initial rake angle increases and the final rake angle decreases, which reduces the fit to observations. Notably, the slip path's upper segment develops convex-down curvature – an effect which becomes stronger with distance along strike (Fig. 8A). This indicates larger stress variation during early slip. While slip path length increases when $\mu_D \leq 0.25$ due to a larger dynamic stress drop, the position of largest slip direction change remains relatively constant with respect to the total path length. When $D_C < 50$ cm the magnitude of surface slip or timing of rake angle change is not modified appreciably.

When $\mu_D \geq 0.25$ or $D_C > 50$ cm, surface slip paths begin to resemble the homogeneous model solution (see Fig. 3A) and in some cases, complexities in the slip path arise (Fig. 8). At all sites, the initial rake angle is too low, and rake angle change is more smoothly varying and occurs earlier compared to observations. Additionally, a sharp kink is observed at Sites 5, 6, and 8 with the opposite sense of convexity compared to observations (Fig. 1B, 8). This is the product of multiple slip fronts evolving near the surface where a zone of enhanced horizontal stress emerges behind the main front. The same behaviour is observed for models with a shallower hypocentre: in this case an additional slip path kink forms but diminishes along strike (Fig. 8C). This suggests that weaker ruptures with lower dynamic stress drops may be associated with more complex slip paths and slickenline shapes.

Changing friction coefficients in the shallow velocity zone alone do not produce appreciable changes in the slip history at the surface. Because effective stress is relatively low in the upper few kilometres of the model, the shallow velocity layers undergo small local stress drops
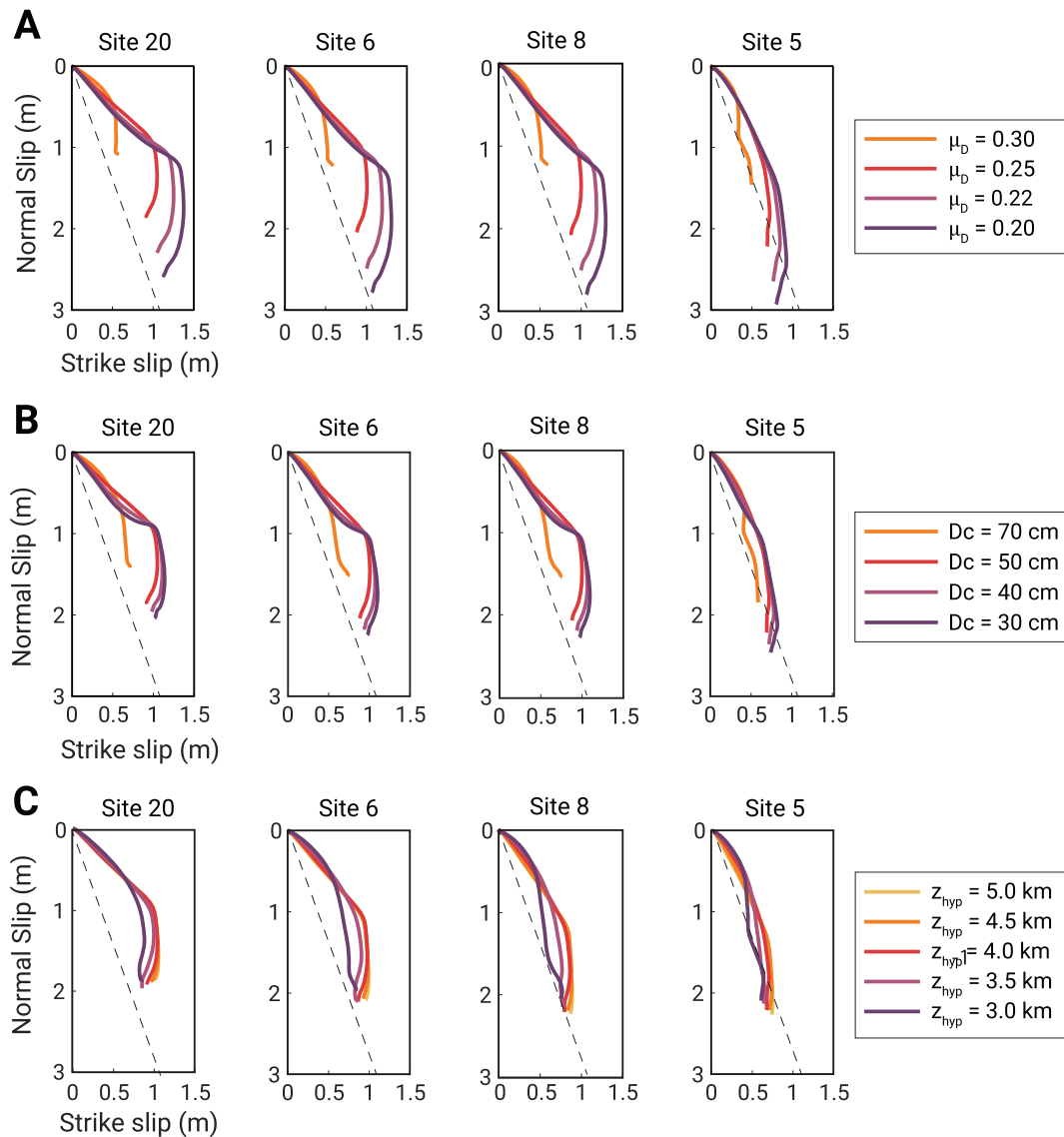
Fig. 8. The sensitivity of surface slip solutions at Sites 5, 6, 8, and 20 where fault variables are changed. In each experiment, the preferred layered velocity model is chosen as a reference and displayed using a red line. The grey dashed line marks the prestress angle ($\theta_0 = -70°$). (A) Decreasing dynamic friction coefficient μ_D produces more slip and the slip path becomes more complex; however, the size of rake angle change between the two slip path segments is not altered significantly. The kink near the slip path's termination related to the model's stoppage phase is more evident for the low μ_D cases where dynamic stress drop is larger. (B) Decreasing D_C weakens total slip direction rotation and introduces more variation in rake angle across the slip path. (C) Shallower hypocentre depths result in more smoothly varying slip paths. When $z = 3$ km, additional kinks in the slip path are present for Sites 5 and 8. This is related to the interference of the model's stoppage phase, the partial arrest of the near-surface, and the interaction with the free surface. (For interpretation of the references to colour in this figure legend, the reader is referred to the web version of this article.)

compared to the fault at depth. Hence, changes in local dynamic stress drop in the shallow velocity zone alone do not influence modelled rupture dynamics appreciably.

4.4. Influence of a free surface

A model with homogeneous velocity structure produces a zone of weak supershear slip near the free surface; such supershear is known to occur in dynamic rupture models where the fault strength is close to zero at the surface (e.g., Kaneko and Lapusta, 2010). In contrast, the rupture front in the layered velocity model splits into two fronts within the shallow velocity layers that produce comparable slip rates. The leading slip front is supershear with respect to V_s of the shallow layers, but subshear to V_s of the underlying halfspace. To better understand the influence of a free surface and modelled supershear on coseismic rake

rotation, we consider cases with uniform prestress, dynamic stress drop, and seismic wavespeed. In this way, the effect of depth-dependent stress or velocity structure upon rupture dynamics is absent and the free surface effect is easier to assess. Here, the aim is not to reproduce observations; instead, we investigate the underlying mechanisms driving coseismic rake rotations in our rupture model.

A pure dip-slip model (where $\theta_0 = -90°$) with uniform prestress and seismic wavespeed produces strong coseismic rake rotation at the surface (Fig. S1). The sense of surface slip path is equivalent to the preferred homogeneous and layered velocity models (Figs. S1, 3B, 3C). Like the homogeneous model, most coseismic rake rotation in the dip-slip model occurs early in the slip path. As expected from mostly model III rupture propagation, no near-surface supershear phase is present (Kaneko and Lapusta, 2010) and slip instead involves a single rupture front. During initial stress loading at Site 20, horizontal traction is of comparable
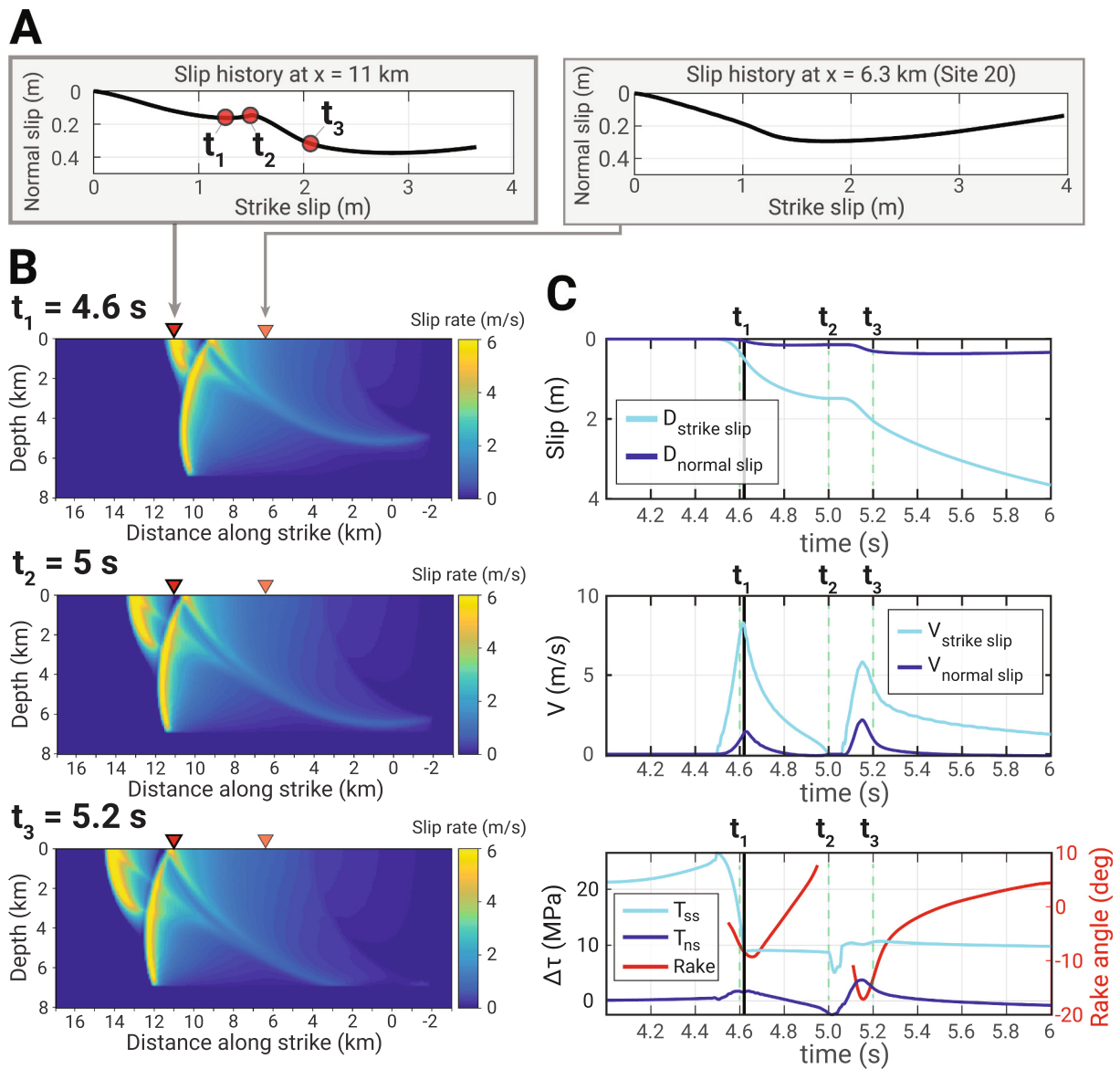
Fig. 9. Fault variables plotted for a pure strike-slip case with uniform stress and seismic wavespeed. (A) Slip paths plotted at two sites on the model surface shows the maximum slip direction change greatly increases with distance along strike. (B) Snapshots of slip rate plotted at three time snapshots show a strong super-shear phase evolving ahead of the main rupture where $z < 4$ km. The kink in the slip path from A relates to the local slip rate minimum between the two slip fronts. Further along strike, the near surface stalls between the arrival of the supershear and main fronts causing a strong change in rake angle when the main front arrives. (C) Plots of slip (m), slip rate (m/s), and shear traction change $\Delta\tau$ (MPa) at $x = 11$ km, $z = 100$ m show that both fronts carry a different ratio of vertical to horizontal stress components and hence induce different rake angle changes. A discontinuity in slip direction results due to the fault temporarily stalling between the two slip fronts, like the thickest case in Fig. 8D.

magnitude to the vertical component. Once the fault breaks, slip rate peaks and after 0.1 s almost all horizontal stress is alleviated (Fig. S1). After the characteristic slip distance is achieved, slip rotates and becomes near-vertical. Rake rotation occurs primarily within the process zone and is controlled mainly by transient horizontal stresses. During the latter part of the slip path, near-surface displacement gently arcs back with right-lateral motion such that the net strike-slip offset is approximately zero (in close alignment with the prestress direction).

A strike-slip model involves a more complex interaction with the free surface which results in slip paths with greater rake angle variation. Fig. 9A shows surface slip at $x = 11$ km and $x = 6.3$ km where fault displacement occurs in two distinct segments separated by a sharp kink. The two slip segments relate to two slip fronts arriving at the surface due to a supershear pulse emerging from the main front (Fig. 9B). The slip path kink for $x = 11$ km occurs once the supershear pulse passes and slip temporarily stalls (Fig. 9B, C). Both fronts cause slip direction to vary with time because they carry small, short-lived vertical stresses (Fig. 9C). Notably, the ratio between horizontal and vertical velocity (and stress) is unique for both fronts; for instance, the supershear pulse contains a greater proportion of horizontal stress which results in less vertical offset and shallower rake angles (Fig. 9A, C). While the sense of curvature is consistent between $x = 11$ km and $x = 6.3$ km, the sharpness of rake angle change increases along strike as the distance between the leading and trailing slip fronts increases. The same set of features are also seen in the thickest layered velocity case (Fig. 7D, F): in both cases rupture front bifurcation causes similar slickenline complexity. However, the strike-slip model's supershear pulse emerges from the rupture front's interaction with the free surface; whereas, in the layered models, the rupture front splits within the shallow velocity layers.

These idealised cases suggest that interactions between rupture and a free surface can greatly complicate the resulting slickenline shapes. When multiple rupture fronts are produced, multiple kinks may be present in the resulting slickenlines. While complicated slickenlines like the $x = 11$ km for the strike-slip case (Fig. 9A) have not yet been documented, we demonstrate that the emergence of multiple slip fronts in the preferred layered velocity model leads to a sharp kink in the Itozawa Fault slickenline records (Figs. 3B, 6).

5. Discussion and conclusions

5.1. Interpreting curved slickenlines of the Fukushima-Hamadori Earthquake

We used relatively simple dynamic rupture models with a fault embedded into a homogeneous or layered elastic half-space and explained detailed, enigmatic observations of slickenlines from a series of fault scarps documented soon after the April 11, 2011, M_w 6.6 Fukushima-Hamadori Earthquake. For the case with homogeneous velocity structure, additional details of the slickenline observations could not be matched despite producing a modelled slip distribution with a comparable slip magnitude to the InSAR-derived slip model (Fig. 3C; Fukushima et al., 2013). Particularly, the majority of rake angle change occurs near the slip path origin (within the modelled fault's process zone), the change is too gradual, and final rake angle is too low compared to the final slip direction of slickenline observations (Fig. 3A). We conclude that a uniform elastic half-space is insufficient for constraining a dynamic rupture model using the Fukushima-Hamadori slickenlines.

Our preferred model with layered velocity structure reproduces both the magnitude of rake rotation and its position late in the slip path (Figs. 1B, 3B). Geophysical observations such as moment magnitude and slip distribution are also well matched. Slickenline observations from the Itozawa West Faults suggest that slip occurs in a dogleg shape – i.e., two segments of relatively constant rake angle are separated by a sharp, unbroken bend. While net rake angle change is not precisely reproduced

at Site 20, path segment lengths at Site 6 are overestimated, and the largely dip-slip displacement at Site 5 is not replicated (this is addressed in Section 5.3), the preferred layered model achieves the desired dogleg shape (Fig. 3B). The dogleg shape results from the rupture front interacting with the shallow low-velocity zone and free surface. Instead of following typical linear slip-weakening behaviour within the process zone, displacement accrues across two discrete slip fronts created by the main rupture front splitting within the uppermost velocity layer (Figs. 5, 6). The initial slip front in the layered model carries faster slip and comprises more of the slip path compared to the initial weak slip episode in the homogeneous model (Fig. 4). For the layered case, significant rake angle change occurs when slip temporarily decelerates during a transition between two peaks in slip rate. These peaks carry different stresses, causing a sharp bend in the latter half of the final slip path (Fig. 6). Overall, patterns in the Fukushima-Hamadori slickenline data are better represented by the preferred layered model.

Our modelling results provide a simple interpretation for the enigmatic Fukushima-Hamadori Earthquake slickenline observations. Otsubo et al. (2013) suggested that the slickenlines' final slip direction aligns with regional stress calculated from stress tensor inversion of events following the M_w 9.0 Tohoku-Oki Earthquake. However, if the prestress direction on the Itozawa fault was aligned with that induced by the Tohoku-Oki earthquake, the net slip direction should have aligned with the prestress direction, as predicted by our model and that of Spudich et al. (1998), rather than the slickenlines' final slip direction. In addition, the reversed curvature of the slickenline on the Yonodake Fault (Kearse and Kaneko, 2020) would not be consistent with the Tohoku-Oki prestress direction. Hence our results demonstrate that the mechanism for coseismic rake rotations may not be specific to the Tohoku-Oki event. Instead, our model relies on a dynamic stress mechanism in association with near-surface rupture dynamics. In our preferred layered models, multiple rupture fronts carrying different orientations of stress changes emerge within a shallow low-velocity medium, leading to significant rake angle changes and curved slickenlines.

Our relatively simple 3-D model extends an existing theory for interpreting slickenline curvature. The main mechanism of rake angle changes in our preferred layered model is different from a previously proposed one in which coseismic rake angles rotate within the process zone (as shown in our homogeneous case) (Andrews, 1994; Spudich et al., 1998). Kearse and Kaneko (2020) demonstrate that slickenline convexities from several surface-breaking earthquakes are consistent with idealised dynamic rupture models. Furthermore, we show that more realistic conditions should be added to Kearse and Kaneko (2020)'s models to extract more information about earthquake dynamics beyond rupture direction. The mechanism of unilateral mixed-mode rupture remains an important component in explaining the broad patterns of slickenline curvature along the Itozawa Fault (Andrews, 1994); however, the emergence of multiple rupture fronts within a shallow low-velocity medium can also lead to significant rake angle changes and curved slickenlines.

5.2. Near surface dynamics in layered model

Our layered model demonstrates that near-surface dynamics can have a significant effect on surface slip. The main rupture front splits within the low-velocity zone where slip rate is enhanced and the separation between slip fronts becomes more pronounced towards the surface. The occurrence of significant rake angle change within a transition between two slip rate peaks is a general observation in all models with layered velocity structure (e.g., Figs. 5, 7). While horizontal stress changes are elevated over the whole low-velocity zone, the first slip episode is most significant in the top few hundred meters where the reflected rupture front constructively interferes with the main front, creating strong slip in addition to elevated horizontal stress (Figs. 5, 6). At depths below ~200 m, rake rotation occurs early in the slip path in a

similar manner to the homogeneous case (Fig. 6B). Here, the ratio of local dynamic stresses to local absolute stress drop becomes smaller as confining stresses increase, which act to decrease the magnitude of coseismic rake rotations (Spudich et al., 1998). This suggests that slickenline shape is most sensitive to rupture dynamics near the Earth's surface. Likewise, our ability to fit detailed geological observations using our modelling framework is sensitive to rupture propagation within the medium's near-surface.

We find that near-surface rupture dynamics and resulting slickenline shapes depend on the details of shallow velocity structure. While changing parameters in the linear slip-weakening law can increase the intensity of the slip path kink, these changes do not improve the fit to observations (Section 4.3). Models with a greater dynamic stress drop (Fig. 8) cause more rake angle variation near the surface (e.g., multiple

inflection points) because their rupture fronts carry larger dynamic stresses sourced from strong energy radiation at depth and because fault strength near the surface is relatively small (Guatteri and Spudich, 1998). However, changes in the shallow velocity structure have the greatest control on the surface slip solution (Fig. 7): the timing of curvature and size of rake rotation is most sensitive to the shallow velocity structure and how the main rupture front interacts with it. Hence, in terms of interpreting the details of surface slip paths, the sense of curvature depends on prestress and rupture directions (Kearse and Kaneko, 2020), but the shape, net rake rotation, and the intensity of curvature are controlled primarily by near-surface dynamics.

The shallow velocity layers could represent a local impedance contrast between a metamorphic cover sequence and granitic basement (Mizoguchi et al., 2012; Otsubo et al., 2013; Geological Survey of Japan,
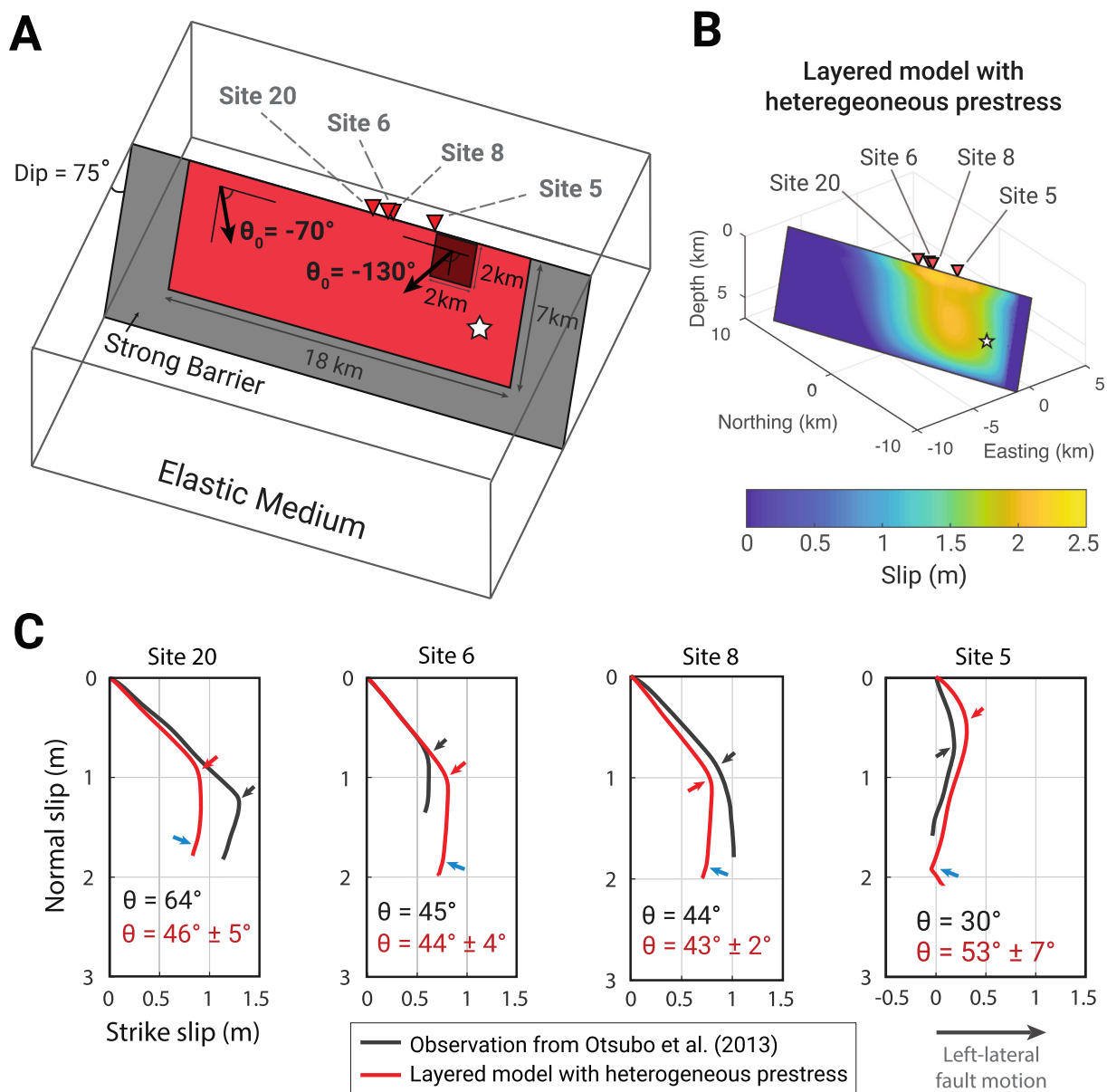
Fig. 10. (A) A 2-km by 2-km fault patch with a prestress of −130 ° is added to the model setup from Fig. 2. The patch sits adjacent to Site 5 to create a local deviation in slip direction. (B) The resulting slip distribution largely resembles the InSAR-derived solution, though, the magnitude of slip is hampered around the fault patch. (C) Surface slip more closely resembles the Site 5 observation. While the initial rake angle is too shallow and net rake rotation is overestimated, the final rake angle and slickenline shape are more consistent with observations. Furthermore, for Site 5, the timing of maximum rake angle change in modelled and observed slip paths (shown by the red and grey arrows respectively) is closer. The blue arrow shows the arrival of the model's stopping phase. Net rake rotation at other sites has not changed appreciably. (For interpretation of the references to colour in this figure legend, the reader is referred to the web version of this article.)

2003); however, we emphasise that relating changes in velocity structure to local geology is beyond the scope of this study. Instead, our results are intended to demonstrate the sensitivity of rupture dynamics to the modelled velocity structure itself and create a preliminary investigation into the general behaviour of rupture front due to the combined effect of shallow (upper few kms) impedance contrasts and the free surface.

5.3. Model limitations

In this study, we assume a planar fault with uniform or smoothly varying friction parameters for simplicity; however, heterogeneity in fault structure or prestress are known to influence earthquake rupture dynamics (e.g., Harris and Day, 1999; Ripperger et al., 2007; Dunham et al., 2011; Perrin et al., 2016) and could complicate slip paths and hence slickenline formed at individual sites. Between Sites 6 and 8 (separated by 100 m), the difference in final rake angle of ~15° and the large difference in total slip of ~0.5 m might be explained by the effect of non-planar fault geometry (e.g., Milliner et al., 2016). Complexity in slickenline data was documented following the 2016 Kaikoura earthquake, where rake rotations distinct from the pattern of curvature observed on relatively linear fault segments are observed at sharp fault bends and stepovers (Kearse et al., 2019). Likewise, the large discrepancy between observed and modelled slickenlines at Site 5 (Fig. 3) may be due to local stress heterogeneities. To test if prestress heterogeneities could account for the discrepancy between the preferred layered model and observation, we consider an additional case using a layered model in which a 2-km by 2-km fault patch of prestress orientated at −130 ° is imposed near Site 5 (Fig. 10). The resulting fit to the observed slickenline at Site 5 greatly improves while the fit to rest of the slickenline data remains satisfactory (Fig. 10). This result suggests that local heterogeneities in prestress, which could be induced by non-planar fault geometry, can be an important factor in explaining complex slickenline records.

In this study, we assume that the frictional resistance is isotropic and the same in all directions at a point on the fault. Anisotropic friction, which could result from fault roughness (e.g., Power et al., 1987; Toy et al., 2017), might influence temporal changes in rake rotation; however, examining models that account for anisotropic frictional resistance remains a subject of future work.

Our models assume purely elastic materials without accounting for off-fault, distributed deformation. Several studies suggest that inelastic off-fault deformation during rupture propagation can limit peak slip velocity at the rupture front or delay or prevent supershear rupture propagation (e.g., Andrews, 2005; Ma, 2008). Since the confining stress is relatively low near the surface, the inelastic zone can broaden at shallow depths (Ma, 2008; Kaneko and Fialko, 2011). If inelastic response becomes progressively important at shallow depths, such response is likely to influence the shape and characteristic of slickenlines. Understanding the effect of inelastic, off-fault response on slickenline shape remains a subject for future work.

5.4. Possibility to resolve near-surface rupture dynamics using slickenline observations

Our results indicate that slickenline observations could constrain near-surface rupture evolution. Our preferred layered model produces a distinct surface slip path that provides the best replication of observed slickenlines out of the models tested. Moreover, such surface slip paths indicate the emergence of multiple slip fronts in the near-surface during the Fukushima-Hamadori Earthquake. Previous theoretical studies reported the potential occurrence of supershear rupture propagation on strike-slip faults caused by the Earth's free surface (e.g., Aagaard et al., 2001; Kaneko et al., 2008; Kaneko and Lapusta, 2010; Hu et al., 2019). While such near-surface supershear rupture has not yet been observed for any surface-breaking earthquakes to date, our results in Section 4.4

may point towards the potential for slickenlines to preserve the occurrence of supershear rupture propagation at shallow depths. Our results indicate that observations of fault slickenlines can supplement seismological studies of earthquake dynamics beyond traditional datasets.

Our experiments in varying dynamic friction (Fig. 8), which induce greater slip magnitude, show that net rake rotation is relatively independent to larger events and the sharp change in rake occurs in roughly the same position with respect to the total displacement. Hence, our model is likely to produce consistent findings for larger ruptures. For smaller events, while complications in slip path complexity are present, rake rotations are still produced and namely the sense of convexity remains consistent with that expected for the rupture direction (i.e., as suggested in Kearse et al., 2020).

Our results call for careful and detailed observations of slickenlines after surface-breaking earthquakes, as the details of slickenline shape provide information about near-surface rupture dynamics. Details such as the timing and sharpness of rake rotation do not solely provide information for understanding the rupture process at seismogenic depths as they largely capture the influence of the rupture front interacting with shallow velocity layers and the free surface. Hence, recording slip direction changes over the entire slip path are important in constraining the progression of shallow rupture. Furthermore, if multiple near-surface rupture fronts are present in earthquakes, this could influence slip behaviour and create distinct slickenline shapes that can be identified in the field, although we acknowledge that such on-fault observations are not yet common. A future goal is to collect enough curved slickenline observations to learn whether multiple rupture fronts are a widespread phenomenon. This requires careful observation for sharp changes in slickenline angle, and how slip varies with time over the complete slip path, and if slip patterns are systematic over the length of surface ruptures.

Author contributions

YK and JK designed preliminary numerical experiments. CM performed simulations, produced all the figures, and drafted the manuscript. All the authors contributed to interpreting the results and producing the manuscript.

Declaration of Competing Interest

The authors declare that they have no known competing financial interests or personal relationships that could have appeared to influence the work reported in this paper.

Acknowledgements

Appendix A. Supplementary data

Supplementary data to this article can be found online at https://doi.org/10.1016/j.tecto.2021.228834.

References

Aagaard, B.T., Hall, J.F., Heaton, T.H., 2001. Characterization of near-source ground motions with earthquake simulations. Earthquake Spectra 17, 177–207. URL:

Ampuero, J.P., 2002. Etude physique et numérique de la nucléation des séismes. Ph.D. thesis. University of Paris VII Paris.

Andrews, D.J., 1994. Dynamic growth of mixed-mode shear cracks. Bull. Seismol. Soc. Am. 84, 1184–1198. URL: https://pubs.geoscienceworld.org/ssa/bssa/article-pdf/84/4/1184/2708132/BSSA0840041184.pdf.

Andrews, D.J., 2005. Rupture dynamics with energy loss outside the slip zone. J. Geophys. Res. Solid Earth 110, 1–14. URL:

Avagyan, A., Ritz, J., Karakhanian, A., Philip, H., 2003. Dual near-surface rupturing mechanism during the 1988 Spitak earthquake (Armenia). Nat. Acad. Sci. Republ. Armenia 56, 14–19. URL: http://earth.asj-oa.am/3176/.

Bizzarri, A., Cocco, M., 2003. Slip-weakening behavior during the propagation of dynamic ruptures obeying rate- and state-dependent friction laws. J. Geophys. Res. 108 https://doi.org/10.1029/2002jb002198.

Bizzarri, A., Cocco, M., 2005. 3D dynamic simulations of spontaneous rupture propagation governed by different constitutive laws with rake rotation allowed. Ann. Geophys. 48, 279–299.

Dominguez, S., Avouac, J.-P., Michel, R., 2003. Horizontal coseismic deformation of the 1999 Chi-Chi earthquake measured from SPOT satellite images: implications for the seismic cycle along the western foothills of central Taiwan. J. Geophys. Res. Solid Earth 108. https://doi.org/10.1029/2001jb000951. URL: https://agupubs.onlinelibrary.wiley.com/doi/full/10.1029/2001JB000951.

Dunham, E.M., Belanger, D., Cong, L., Kozdon, J.E., 2011. Earthquake ruptures with strongly rate-weakening friction and off-fault plasticity, part 2: nonplanar faults. Bull. Seismol. Soc. Am. 101, 2308–2322. https://doi.org/10.1785/0120100076.

Fialko, Y., Simons, M., Agnew, D., 2001. The complete (3-D) surface displacement field in the epicentral area of the 1999 Mw 7.1 Hector Mine Earthquake, California, from space geodetic observations. Geophys. Res. Lett. 28, 3063–3066. URL: http://doi.wiley.com/10.1029/2001GL013174. https://doi.org/10.1029/2001GL013174.

Fujiwara, H., Kawai, S., Aoi, S., Morikawa, N., Senna, S., Azuma, H., Ooi, M., Hao, K.X., Hasegawa, N., Maeda, T., et al., 2012. Some improvements of seismic hazard assessment based on the 2011 Tohoku earthquake. In: Technical Note of the National Research Institute for Earth Science and Disaster Prevention, p. 379.

Fukushima, Y., Takada, Y., Hashimoto, M., 2013. Complex ruptures of the 11 April 2011 Mw 6.6 Iwaki earthquake triggered by the 11 march 2011 Mw 9.0 Tohoku earthquake, Japan. Bull. Seismol. Soc. Am. 103, 1572–1583. https://doi.org/10.1785/0120120140.

Fukuyama, E., Suzuki, W., 2016. Near-fault deformation and D″ during the 2016 Mw 7.1 Kumamoto earthquake. Earth Planets Space 68, 194. https://doi.org/10.1186/s40623-016-0570-6.

Geological Survey of Japan, 2003. Geological Map of Japan 1:1000000, 3rd ed.

Guatteri, M., Spudich, P., 1998. Coseismic temporal changes of slip direction: the effect of absolute stress on dynamic rupture. Bull. Seismol. Soc. Am. 88, 777–789.

Harris, R.A., Day, S.M., 1999. Dynamic 3D simulations of earthquakes on en echelon faults. Geophys. Res. Lett. 26, 2089–2092. URL:

Harris, R.A., Barall, M., Archuleta, R., Dunham, E., Aagaard, B., Ampuero, J.P., Bhat, H., Cruz-Atienza, V., Dalguer, L., Dawson, P., Day, S., Duan, B., Ely, G., Kaneko, Y., Kase, Y., Lapusta, N., Liu, Y., Ma, S., Oglesby, D., Olsen, K., Pitarka, A., Song, S., Templeton, E., 2009. The SCEC/USGS dynamic earthquake rupture code verification exercise. Seismol. Res. Lett. 80, 119–126. https://doi.org/10.1785/gssrl.80.1.119.

Harris, R.A., Aagaard, B., Barall, M., Ma, S., Roten, D., Olsen, K., Duan, B., Liu, D., Luo, B., Bai, K., Ampuero, J.P., Kaneko, Y., Gabriel, A.A., Duru, K., Ulrich, T., Wollherr, S., Shi, Z., Dunham, E., Bydlon, S., Zhang, Z., Chen, X., Somala, S.N., Pelties, C., Tago, J., Cruz-Atienza, V.M., Kozdon, J., Daub, E., Aslam, K., Kase, Y., Withers, K., Dalguer, L., 2018. A suite of exercises for verifying dynamic earthquake rupture codes. Seismol. Res. Lett. 89, 1146–1162. https://doi.org/10.1785/0220170222.

Hikima, K., 2012. Rupture process of the April 11, 2011 Fukushima Hamadori Earthquake (Mj 7.0). J. Seismol. Soc. Japan 64, 243–256.

Hu, F., Oglesby, D.D., Chen, X., 2019. The sustainability of free-surface-induced supershear rupture on strike-slip faults. Geophys. Res. Lett. 46, 9537–9543. URL:

Ida, Y., 1972. Cohesive force across the tip of a longitudinal-shear crack and Griffith's specific surface energy. J. Geophys. Res. 77, 3796–3805. https://doi.org/10.1029/jb077i020p03796.

Imanishi, K., Ando, R., Kuwahara, Y., 2012. Unusual shallow normal-faulting earthquake sequence in compressional northeast Japan activated after the 2011 off the Pacific coast of Tohoku earthquake. Geophys. Res. Lett. 39 https://doi.org/10.1029/2012GL051491.

Kaneko, Y., Fialko, Y., 2011. Shallow slip deficit due to large strike-slip earthquakes in dynamic rupture simulations with elasto-plastic off-fault response. Geophys. J. Int. 186, 1389–1403. https://doi.org/10.1111/j.1365-246X.2011.05117.x.

Kaneko, Y., Lapusta, N., 2010. Supershear transition due to a free surface in 3-D simulations of spontaneous dynamic rupture on vertical strike-slip faults. Tectonophysics 493, 272–284. https://doi.org/10.1016/j.tecto.2010.06.015.

Kaneko, Y., Lapusta, N., Ampuero, J.P., 2008. Spectral element modeling of spontaneous earthquake rupture on rate and state faults: Effect of velocity-strengthening friction at shallow depths. J. Geophys. Res. Solid Earth 113. https://doi.org/10.1029/2007JB005553.

Kaneko, Y., Ampuero, J.P., Lapusta, N., 2011. Spectral-element simulations of long-term fault slip: Effect of low-rigidity layers on earthquake-cycle dynamics. J. Geophys. Res. Solid Earth 116. https://doi.org/10.1029/2011JB008395.

Kaneko, Y., Fukuyama, E., Hamling, I.J., 2017. Slip-weakening distance and energy budget inferred from near-fault ground deformation during the 2016 Mw 7.8 Kaikōura earthquake. Geophys. Res. Lett. 44, 4765–4773. URL:

Kato, A., Sakai, S., Obara, K., 2011. A normal-faulting seismic sequence triggered by the 2011 off the Pacific coast of Tohoku Earthquake: wholesale stress regime changes in the upper plate. Earth Planets Space 63, 745–748. https://doi.org/10.5047/eps.2011.06.014.

Kearse, J., Kaneko, Y., 2020. On-fault geological fingerprint of earthquake rupture direction. J. Geophys. Res. Solid Earth 125, e2020JB019863. https://doi.org/10.1029/2020JB019863.

Kearse, J., Little, T.A., van Dissen, R.J., Barnes, P.M., Langridge, R., Mountjoy, J., Ries, W., Villamor, P., Clark, K.J., Benson, A., Lamarche, G., Hill, M., Hemphill-Haley, M., 2018. Onshore to offshore ground-surface and seabed rupture of the Jordan–Kekerengu–Needles fault network during the 2016 Mw 7.8 Kaikōura earthquake, New Zealand. Bull. Seismol. Soc. Am. 108, 1573–1595. https://doi.org/10.1785/0120170304.

Kearse, J., Kaneko, Y., Little, T., Van Dissen, R., 2019. Curved slickenlines preserve direction of rupture propagation. Geology 47, 838–842. https://doi.org/10.1130/G46563.1.

Kobayashi, T., Tobita, M., Koarai, M., Okatani, T., Suzuki, A., Noguchi, Y., Yamanaka, M., Miyahara, B., 2012. InSAR-derived crustal deformation and fault models of normal faulting earthquake (Mj 7.0) in the Fukushima-Hamadori area. Earth. Planets Space 64, 1209–1221. https://doi.org/10.5047/eps.2012.08.015.

Koketsu, K., Miyake, H., Suzuki, H., 2012. Japan Integrated Velocity Structure Model Version 1. In: Proceedings of the 15th World Conference on Earthquake Engineering. Lisbon. URL: http://www.iitk.ac.in/nicee/wcee/article/WCEE2012_1773.pdf.

Ma, S., 2008. A physical model for widespread near-surface and fault zone damage induced by earthquakes. Geochem. Geophys. Geosyst. 9 https://doi.org/10.1029/2008GC002231 n/a–n/a. URL: http://doi.wiley.com/10.1029/2008GC002231.

Milliner, C.W., Sammis, C., Allam, A.A., Dolan, J.F., Hollingsworth, J., Leprince, S., Ayoub, F., 2016. Resolving fine-scale heterogeneity of co-seismic slip and the relation to fault structure. Sci. Rep. 6, 1–9. URL:

Mizoguchi, K., Uehara, S.I., Ueta, K., 2012. Surface fault ruptures and slip distributions of the M w 6.6 11 April 2011 Hamadori, Fukushima prefecture, Northeast Japan, earthquake. Bull. Seismol. Soc. Am. 102, 1949–1956. https://doi.org/10.1785/0120110308.

Okada, T., Yoshida, K., Ueki, S., Nakajima, J., Uchida, N., Matsuzawa, T., Umino, N., Hasegawa, A., 2011. Shallow inland earthquakes in NE Japan possibly triggered by the 2011 off the Pacific coast of Tohoku Earthquake. Earth Planets Space 63, 749–754. https://doi.org/10.5047/eps.2011.06.027.

Otsubo, M., Shigematsu, N., Imanishi, K., Ando, R., Takahashi, M., Azuma, T., 2013. Temporal slip change based on curved slickenlines on fault scarps along Itozawa fault caused by 2011 Iwaki earthquake, northeast Japan. Tectonophysics 608, 970–979. https://doi.org/10.1016/j.tecto.2013.07.022.

Otsubo, M., Miyakawa, A., Imanishi, K., 2018. Normal-faulting stress state associated with low differential stress in an overriding plate in northeast Japan prior to the 2011 Mw 9.0 Tohoku earthquake. Earth Planets Space 70. https://doi.org/10.1186/s40623-018-0813-9.

Otsuki, K., Minagawa, J., Aono, M., Ohtake, M., 1997. On the curved striations of Nojima seismic fault engraved at the 1995 Hyogoken-Nambu Earthquake, Japan. Zisin 49, 451–460.

Palmer, A.C., Robert Rice, J., 1973. The growth of slip surfaces in the progressive failure of over-consolidated clay. Proc. R. Soc. Lond A Math. Phys. Sci. 332, 527–548. https://doi.org/10.1098/rspa.1973.0040.

Perrin, C., Manighetti, I., Ampuero, J.P., Cappa, F., Gaudemer, Y., 2016. Location of largest earthquake slip and fast rupture controlled by along-strike change in fault structural maturity due to fault growth. J. Geophys. Res. Solid Earth 121, 3666–3685. URL:

Pitarka, A., Dalguer, L.A., Day, S.M., Somerville, P.G., Dan, K., 2009. Numerical study of ground-motion differences between buried-rupturing and surface-rupturing earthquakes. Bull. Seismol. Soc. Am. 99, 1521–1537. https://doi.org/10.1785/0120080193.

Power, W.L., Tullis, T.E., Brown, S.R., Boitnott, G.N., Scholz, C.H., 1987. Roughness of natural fault surfaces. Geophys. Res. Lett. 14, 29–32. URL:

Ripperger, J., Ampuero, J.-P., Mai, P.M., Giardini, D., 2007. Earthquake source characteristics from dynamic rupture with constrained stochastic fault stress. J. Geophys. Res. Solid Earth 112. https://doi.org/10.1029/2006JB004515. URL: http://doi.wiley.com/10.1029/2006JB004515.

Somerville, P.G., 2003. Magnitude scaling of the near fault rupture directivity pulse. Phys. Earth Planet. Inter. 137, 201–212. https://doi.org/10.1016/S0031-9201(03)00015-3.

Spudich, P., Guatteri, M., Otsuki, K., Minagawa, J., 1998. Use of fault striations and dislocation models to infer tectonic shear stress during the 1995 Hyogo-ken Nanbu (Kobe) earthquake. Bull. Seismol. Soc. Am. 88, 413427. URL: https://pubs.geoscienceworld.org/ssa/bssa/article-pdf/88/2/413/2709377/BSSA0880020413.pdf.

Tanaka, M., Asano, K., Iwata, T., Kubo, H., 2014. Source rupture process of the 2011 Fukushima-ken Hamadori earthquake: how did the two subparallel faults rupture? Earth Planets Space 66. https://doi.org/10.1186/1880-5981-66-101.

Toda, S., Tsutsumi, H., 2013. Simultaneous reactivation of two, subparallel, inland normal faults during the Mw 6.6 11 April 2011 Iwaki earthquake triggered by the M w 9.0 Tohoku-oki, Japan, Earthquake. Bull. Seismol. Soc. Am. 103, 1584–1602. https://doi.org/10.1785/0120120281.

Toda, S., Stein, R.S., Lin, J., 2011. Widespread seismicity excitation throughout central Japan following the 2011 M=9.0 Tohoku earthquake and its interpretation by Coulomb stress transfer. Geophys. Res. Lett. 38 https://doi.org/10.1029/2011GL047834.

Toy, V.G., Niemeijer, A., Renard, F., Morales, L., Wirth, R., 2017. Striation and slickenline development on quartz fault surfaces at crustal conditions: Origin and effect on friction. J. Geophys. Res. Solid Earth 122, 3497–3512. URL:

Xu, S., Nieto-Samaniego, A., Alaniz-Àlvarez, S.A., 2013. Origin of superimposed and curved slickenlines in San Miguelito range, Central México. Geol. Acta 11, 103–112. URL: https://ddd.uab.cat/record/106076.

Yoshida, K., Hasegawa, A., Okada, T., 2015. Spatially heterogeneous stress field in the source area of the 2011 Mw 6.6 Fukushima-Hamadori earthquake, NE Japan, probably caused by static stress change. Geophys. J. Int. 201, 1062–1071. https://doi.org/10.1093/gji/ggv068.

Coseismic slickenlines record the emergence of multiple rupture fronts during a surface-breaking earthquake Supplementary Material

Clarrie Macklin[a], Yoshihiro Kaneko[a,c,*], Jesse Kearse[a,b]

[a]*GNS Science, 1 Fairway Drive, Lower Hutt, New Zealand*
[b]*Victoria University of Wellington, Kelburn Parade, Wellington, New Zealand*
[c]*Graduate School of Science, Kyoto University, Kyoto, Japan*

1. Parameters explored for the homogeneous seismic wavespeed test

Table S1: Parameters explored for the homogeneous seismic wavespeed test

Parameter	Description	Range tested	Units (SI)
D_C	Slip-weakening distance	0.2–2.0	m
μ_S	Static friction coefficient	0.75	
μ_D	Dynamic friction coefficient	0.05–0.40	
C	Frictional cohesion	0.2–2	MPa
θ_0	Prestress angle	$-90° - -50°$	degrees
z_{hyp}	Hypocentre depth	3–5	km

*Corresponding author
Email address:* `y.kaneko@gns.cri.nz` (Yoshihiro Kaneko)

2. Parameters explored for the layered test

Table S2: Parameters explored for the layered model

Parameter	Description	Range tested	Units (SI)
D_C	Slip-weakening distance	0.3–0.7	m
μ_S	Static friction coefficient	0.75	
μ_D	Dynamic friction coefficient	0.20–0.30	
z_{hyp}	Hypocentre depth	3–5	km

3. Description of calculating rake angle rotation

Net rake rotation is calculated using the difference in rake angle between linear fits to the upper and lower path segments. Since slip direction changes continuously for the homogeneous model, at least in the first $\sim 1\,\mathrm{m}$ of slip, we define maximum and minimum bounds on what part of the slip path to include and the maximum angle change is given by fitting the start and end of slip paths only, and the minimum by dividing the slip path in two at the point of inflection and fitting all points either side. The uncertainty range corresponds to the difference in total angle change between these two approaches

4. Dip-slip case with uniform prestress
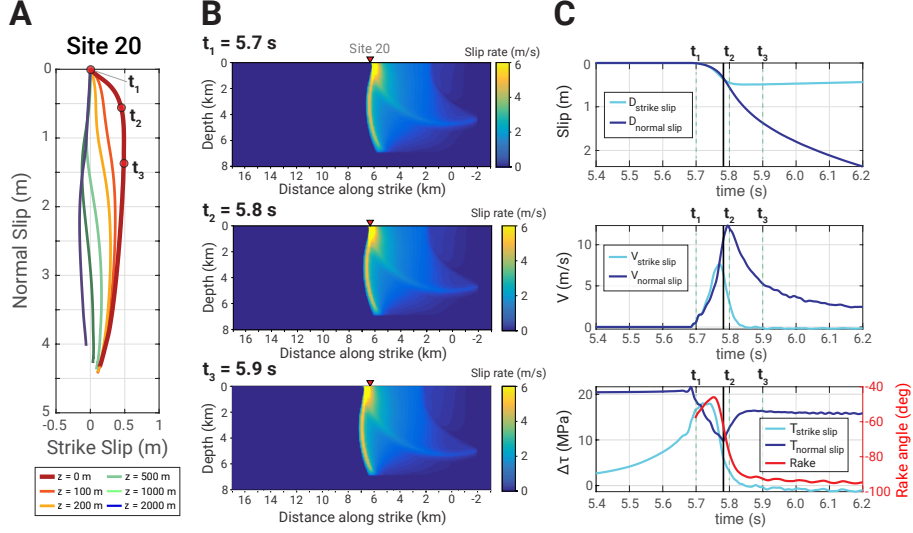
Figure S1: Fault variables plotted for the dip-slip model with uniform prestress and seismic wavespeed. (**A**) Surface slip is plotted at Site 20 ($x = 6.3\,\mathrm{km}$) for $z = 0\,\mathrm{m}$–$2000\,\mathrm{m}$. Horizontal displacement in the first $0.1\,\mathrm{s}$ is greatly enhanced at the free surface and decays quickly with depth. By $z = 100\,\mathrm{m}$, the change in slip direction near the start of the slip path has largely disappeared. Below this, several changes in slip direction occur due to the passing of both the main and reflected slip fronts. (**B**) Three snapshots of slip rate (m/s) show a single strong slip front propagating across the rupture region with a reflected slip font following behind. (**C**) Slip (m), slip rate (m/s), and shear traction change $\Delta\tau$ (MPa) are plotted from top to bottom, respectively. The black bar shows where slip has exceeded the characteristic distance D_C. Variation in rake angle occur early in the slip path and are largely related to transient horizontal stresses carried by the rupture front.